Bulletin of the Seismological Society of America, Vol. XX, No. XX, pp. –, – 2018, doi: 10.1785/0120170259

A New Seismic Hazard Model for Ecuador

by C. Beauval, J. Marinière, H. Yepes, L. Audin, J.-M. Nocquet,* A. Alvarado, S. Baize, J. Aguilar, J.-C. Singaucho, and H. Jomard

Abstract We present a comprehensive probabilistic seismic hazard study for Ecuador, a country exposed to a high seismic hazard from megathrust subduction earthquakes and moderate-to-large shallow crustal earthquakes. Building on knowledge gained during the last decade about historical and contemporary seismicity, active tectonics, geodynamics, and geodesy, several alternative earthquake recurrence models have been developed. We propose an areal seismic zonation for the seismogenic crustal, inslab, and interface sources, modified from Yepes *et al.* (2016), to account for the information gained after the 2016 M_w 7.8 Pedernales megathrust earthquake. Three different earthquake catalogs are used to account for uncertainties in magnitude–frequency distribution modeling. This first approach results in low hazard estimates for some areas near active crustal fault systems with low instrumental seismicity, but where geology and/or geodesy document rapid slip rates and high seismic potential. Consequently, we develop an alternative fault and background model that includes faults with earthquake recurrence models inferred from geologic and/or geodetic slip-rate estimates. The geodetic slip rates for a set of simplified faults are estimated from a Global Positioning System (GPS) horizontal velocity field from Nocquet *et al.* (2014). Various scenarios are derived by varying the percentage of motion that takes place aseismically. Combining these alternative earthquake recurrence models in a logic tree, and using a set of selected ground-motion models adapted to Ecuador's different tectonic settings, mean hazard maps are obtained with their associated uncertainties. At the sites where uncertainties on hazard estimates are highest (difference between 84th and 16th percentiles $> 0.4g$), the overall uncertainty is controlled by the epistemic uncertainty on the source model.

Introduction

During the last decade, the French–Ecuadorian scientific collaboration has produced new results in most of the fields required for a probabilistic seismic hazard assessment (PSHA). Historical earthquakes were studied, providing new locations and magnitudes (Beauval *et al.*, 2010). A homogeneous earthquake catalog was compiled using historical and instrumental earthquake catalogs (Beauval *et al.*, 2013). New insights into active tectonics significantly improved the understanding of the active fault systems in the country (Alvarado *et al.*, 2014, 2016; Baize *et al.*, 2015). A new view of Ecuador's complex geodynamics has been developed, and new seismic source zones for PSHA have been defined (Yepes *et al.*, 2016). Deformation observed through geodetic and seismological measurements led to the development of better detailed plate tectonic models for the region and a better understanding of the Ecuadorian subduction interface's ability to produce large earthquakes (Chlieh *et al.*, 2014; Nocquet *et al.*, 2014, 2016). The 2016 M_w 7.8 Pedernales earthquake, responsible for more than 650 casualties and considerable destruction, was a terrible reminder that most of Ecuador faces a high seismic risk. Aside from subduction zone earthquakes, several strong earthquakes have occurred along the fault system bordering the Interandean Valley during the last 500 years (e.g., 1868 M_w 7.1–7.7 Ibarra earthquake; 1797 M_w 7.5–7.9 Riobamba earthquake; Beauval *et al.*, 2010). Events that occur along shallow crustal faults have the potential to be much more destructive than megathrust events. To limit the number of casualties, buildings should be built or reinforced to resist strong ground motions. The goal of PSHA is to provide authorities with a basis and reference from which ground motions should be considered for earthquake resistant design (earthquake building code for design or retrofit).

PSHA methods were introduced in the late 1960s (Cornell, 1968; Esteva, 1968) and are now considered state-of-the-art methods to estimate seismic hazard in most regional, national, and international seismic regulations (e.g.,

*Also at Institut de Physique du Globe de Paris, Sorbonne Paris Cité, Université Paris Diderot, UMR 7154 CNRS, Paris, France.

Eurocode 8, 2004; U.S. National Seismic Hazard Maps, Petersen *et al.*, 2014). PSHA aims to interpret knowledge about the sources and the magnitudes that may occur in terms of rates of occurrence (source model). Thanks to empirical models, the ground motions produced by these future events can be estimated (ground-motion model [GMM]). The source model and the GMM are then combined to determine the exceedance probabilities of ground-motion levels at sites of interest over future windows of time.

The first Ecuadorian Building Code (EBC) was launched in 1951 after the 1949 M_w 6.4 central Ecuador crustal earthquake (~6000 casualties). Although no seismic hazard calculation was made, earthquake-resistant measures were suggested for retrofitting damaged structures. Important amendments based on the California Uniform Building Code were made in 1976 after the small M_w 6.6 Esmeraldas City interface earthquake, and a single seismic zone was adopted for the country. Several PSHA academic studies were performed in the 1990s (e.g., Bonilla *et al.*, 1992) but the results were not used for establishing zoning. In 2001, the EBC was updated (Código Ecuatoriano de la Construcción [CEC], 2001), as a response to the 1998 M_w 7.1 Bahía de Caráquez interface earthquake. EBC relied on probabilistic seismic hazard calculations (53 areal source zones and two GMMs, one for subduction interface and one for crustal earthquakes), and subdivided the country into four seismic zones. The EBC was updated again in 2015 (Norma Ecuatoriana de la Construcción [NEC], 2015), based on a seismic zoning map outlined from an earlier version of our seismic hazard model, calculated with a trial version of the OpenQuake PSHA software. A new version is expected in light of recommendations still to be drawn from the weak performance of structures during the 2016 M_w 7.8 interface earthquake. The new seismic hazard model presented here will be used to redefine the national seismic zoning map and provide peak ground acceleration (PGA) and associated uncertainty values for design response spectra.

In this study, we describe a comprehensive PSHA calculation for Ecuador, relying on the most up-to-date information available. This article is organized as follows. First, the so-called area model is described, in which we introduce the seismogenic sources, earthquake catalogs, and magnitude–frequency distributions derived for all crustal, interface, and intraslab sources. An alternative fault model is developed, including the crustal faults for which relevant data have been collected. Earthquake recurrence on these fault sources is inferred from geodetic and/or geologic slip rates. GMMs are selected from recently published models. A logic tree is built exploring the uncertainty on the source model and on the prediction of ground motions. Probabilistic seismic hazard is calculated over a grid of rock sites (V_{S30} 760 m/s) that cover the entire country to produce mean probabilistic hazard maps and 16th and 84th percentile hazard maps. Finally, a specific study is led in the cities of Quito, Guayaquil, and Esmeraldas, in order to compare the contributions of source model uncertainty and GMM uncertainty to overall uncertainty.

Area Model

Seismogenic Sources

Yepes *et al.* (2016) proposed a set of seismogenic sources to model earthquake occurrences along crustal shallow faults, at the subduction interface, and inside the slab at depth (Figs. 1 and 2). The crustal area source model encloses the main fault system that delineates the southern border of the North Andean Sliver (NAS; Nocquet *et al.*, 2014; Alvarado *et al.*, 2016). This fault system includes four groups of transpressive structures (namely the Puna, Pallatanga, Cosanga, and Chingual fault systems, Fig. 1). In addition, the Quito-Latacunga thrust fault system is enclosed in a source zone connected in the north to the El Angel strike-slip fault system; whereas the eastern sub-Andean thrust-and-fold belt is split into the wide Cutucu source zone to the south and the Napo source zone to the north (Fig. 1). In addition to the Yepes *et al.* (2016) shallow crustal source zones, two background sources are added to account for the diffuse seismicity off the main fault systems (north and to south of the Puna source, Fig. 1). The intraslab events are grouped into volumes defined at increasing depths to model the dipping slab (Fig. 2). The Grijalva rifted margin separates two different subducting slabs with many more events in the southern part (Farallon slab). The Farallon slab is modeled by four dipping volumes; the Morona zone at 100–130 km depth is the most seismically active. A precise description of the crustal and intraslab sources can be found in Yepes *et al.* (2016).

The subduction interface segmentation has been revised with respect to the one described in the Yepes *et al.* (2016) model after new interpretations emerged following the 16 April 2016 M_w 7.8 Pedernales megathrust earthquake. The strongly coupled Esmeraldas segment, which hosted the 1906 M_w 8.4–8.8 earthquake (Kanamori and McNally, 1982; Di Giacomo *et al.*, 2015; Ye *et al.*, 2016), is now extended 50 km farther to the south (Fig. 1) with respect to the model from Yepes *et al.* (2016). The 2016 M_w 7.8 Pedernales earthquake rupture stopped slightly south of the Esmeraldas source zone southern boundary proposed in Yepes *et al.* (2016) and Nocquet *et al.* (2016). The new Esmeraldas zone includes the entire seismically highly coupled area modeled by Chlieh *et al.* (2014) and Nocquet *et al.* (2016). The Bahia source zone in Yepes *et al.* (2016), south of the Esmeraldas source segment, is thus reduced with respect to the 2016 model and is now called La Plata. It includes a weakly locked corridor as well as a highly locked shallow patch around La Plata island imaged from Global Positioning System (GPS) interseismic velocities (latitude −1.3°; Vallée *et al.*, 2013; Chlieh *et al.*, 2014; Collot *et al.*, 2017). This area appears to release a significant fraction of strain by frequent slow-slip events, possibly precluding the occurrence of large

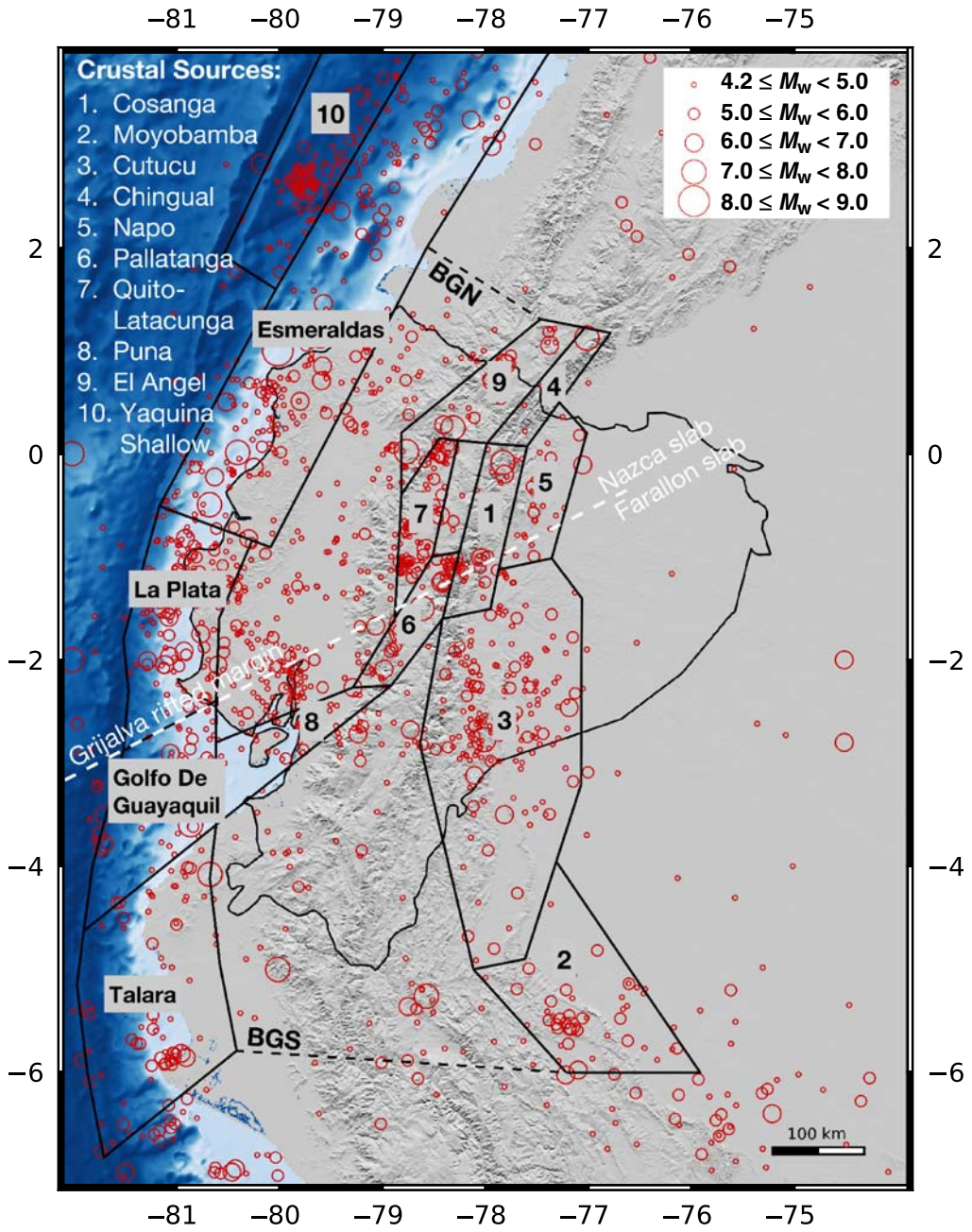

Figure 1. Seismogenic sources: interface-dipping planes and crustal area sources, earthquakes with depth ≤ 35 km (Beauval *et al.*, 2013; BSSA2013 catalog, see the Earthquake Catalogs section). The color version of this figure is available only in the electronic edition.

earthquakes (Collot *et al.*, 2017). South of the Guayaquil Gulf, the previous Talara source zone showing weak to negligible interplate locking (Nocquet *et al.*, 2014; Villegas-Lanza *et al.*, 2016) is now split into two smaller zones, Golfo de Guayaquil (a transition zone) and Talara. Its southern limit corresponds to the southwestern continuation of the Tumbes-Zorritos detachment system and the Banco Peru fault (Witt *et al.*, 2006) as the possible southern boundary of the NAS in the Gulf of Guayaquil area. Overall, the proposed changes with respect to Yepes *et al.* (2016) result in a zonation consistent with the interseismic coupling information derived from GPS data and the history of large subduction earthquakes.

Earthquake Catalogs

Three Alternative Earthquake Catalogs. An earthquake catalog is required to model magnitude–frequency distributions within each source zone. Building a unified and homogeneous earthquake catalog for seismic hazard assessment is a difficult task that requires meticulous work. The resulting catalog inevitably suffers from significant uncertainties because

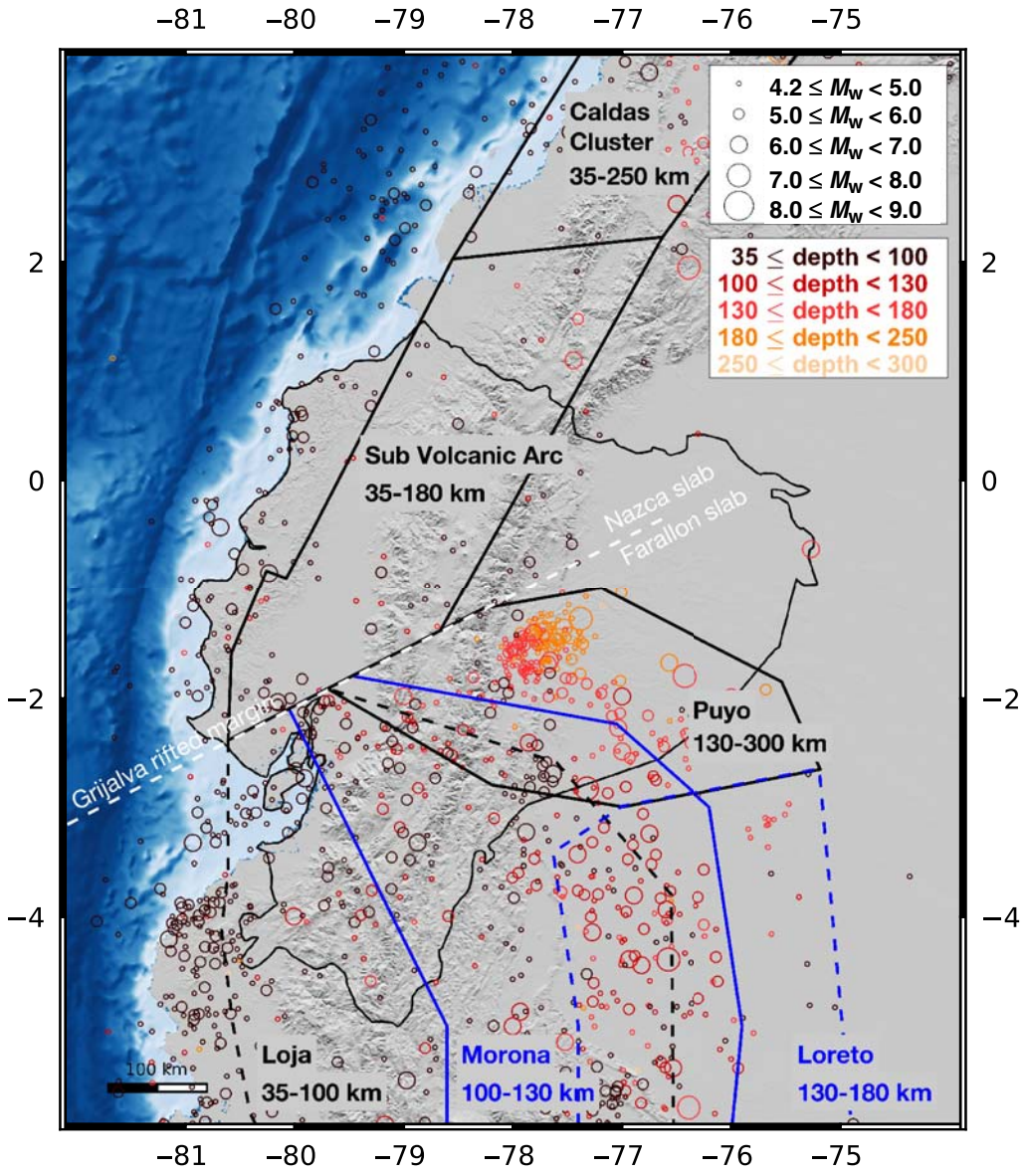

Figure 2. Seismogenic sources: intraslab sources (volumes), earthquakes deeper than 35 km (BSSA2013 catalog, see the Earthquake Catalogs section). The color version of this figure is available only in the electronic edition.

data that encompass different time periods, from historical and early instrumental earthquakes to events recorded by advanced instrumental networks, are gathered. Alternative reliable catalogs provide alternative recurrence models and a means to quantify the uncertainty on the recurrence. To explore uncertainty in the earthquake catalog, three alternative earthquake catalogs are developed for the spatial window −7° to +4° in latitude, and −82° to −74° in longitude.

- The Beauval *et al.* (2013; hereafter, BSSA2013) homogeneous and unified earthquake catalog, covering the time window 1541–2009, was used in the PSHA for Quito (Beauval *et al.*, 2014). It includes historical and instrumental data from local and global earthquake catalogs. As described in detail in Beauval *et al.* (2013), work has been performed to merge the different reliable catalogs available at the time, to identify the best solutions in magnitude and location, and to homogenize earthquake magnitudes.
- The International Seismological Centre (ISC)-based earthquake catalog, covering the time window 1901–2014 (Table 1), is built from three global instrumental catalogs: the new global ISC-Global Earthquake Model (GEM) catalog (Storchak *et al.*, 2015), the ISC event catalog, and the Global Centroid Moment Tensor (CMT) catalog. This catalog is more homogeneous in terms of magnitude than the BSSA2013 catalog. It is possible to ignore historical earthquakes because recurrence models rely mostly on the

Table 1
International Seismological Centre (ISC)-Based Earthquake Catalog, All Events with Proxy $M_w \geq 4.2$

Catalog	Author	Type Magnitude	Minimum Magnitude	Maximum Magnitude	Minimum Year	Maximum Year	Total Number of Events
GEM	Various	M_w	5.1	7.8	1920	2000	106
GEM	Global CMT	M_w	5.56	8.09	1965	2013	101
GEM supp	Various	Proxy M_w	6.12	8.35	1906	1928	5
Global CMT	Global CMT	M_w	4.8	5.8	1977	2013	169
ISC	Global CMT	M_w	4.9	6.3	2007	2014	7
ISC	ISC	Proxy M_w from MS	6.4	6.5	1952	1953	2
ISC	ISC	Proxy M_w from m_b*	4.28	6.16	1964	2014	2022*
ISC	NEIC	Proxy M_w from M_s	4.2	4.2	1990	1990	1
ISC	NEIC	Proxy M_w from m_b*	4.28	5.6	1985	2014	25*
ISC	NEIS	Proxy M_w from m_b*	4.28	5.21	1971	1978	44*
ISC	USCGS	Proxy M_w from m_b*	4.28	6.02	1965	1965	18*
ISC	ABE1	m_b surrogate for M_w	7.1	7.2	1917	1937	2
ISC	AN2	M_s surrogate for M_w	7	7	1907	1912	2
ISC	P&S	M_w	7.2	7.2	1901	1901	1
ISC	PAS	M_s surrogate for M_w	6.5	6.8	1954	1958	4
ISC	PAS	M_s surrogate for M_w	5.5	6.8	1930	1950	21

GEM, Global Earthquake Model; CMT, Centroid Moment Tensor; NEIC/NEIS, National Earthquake Information Center; USCGS, United States Coast and Geodetic Survey; ABE1, Abe (1981); AN2, Abe and Noguchi (1983); P&S, Pacheco and Sykes (1992); PAS, Gutenberg and Richter (1965).

*Magnitude m_b converted in M_w applying $M_w = \exp(0.741 + 0.210 m_b) - 0.785$ (Lolli *et al.*, 2014, global equation).

most populated magnitude bins based on the instrumental part of the catalog (however, historical earthquakes are considered when proposing maximum magnitudes). For earthquakes with m_b and M_s teleseismic magnitudes, M_w proxies are estimated by applying Lolli *et al.* (2014) global conversion equations. Catalog details are provided in the second part of this section.

- The National Earthquake Information Center (NEIC)-based catalog is provided by the NEIC of the U.S. Geological Survey (see Data and Resources). It includes the NEIC solutions, as well as solutions from other global and local catalogs. Since the 1970s, the NEIC delivers solutions earlier and uses fewer stations than the ISC. Although it is not as complete as the ISC Bulletin, it advantageously covers the time window 1900–2017, including the 2016 megathrust event. For earthquakes with m_b and M_s teleseismic magnitudes, M_w proxies are estimated applying Lolli *et al.* (2014) conversion equations.

In the final logic tree, a weight of 0.5 is attributed to the BSSA2013 catalog branch because this catalog is considered the most complete in terms of both instrumental and historical earthquakes. A weight of 0.4 is attributed to the ISC-based catalog branch, as it contains improved locations and magnitudes for instrumental events with $M_w \geq 5.5$. Lastly, a weight of 0.1 is attributed to the NEIC-based catalog branch. When modeling earthquake recurrence in the source zones, the NEIC-based catalog appeared to be the least complete. The ISC-based catalog and the NEIC-based catalog are declustered and completeness time periods are identified using the same procedures as for the BSSA2013 catalog (see details in Beauval *et al.* 2013). Around 20% of clustered events are discarded from the ISC-based and NEIC-based catalogs. Table 2 summarizes the time period of completeness obtained from graphics that represent the cumulative number of events versus time.

Building the ISC-Based Catalog. The final homogenized ISC-based catalog is displayed in Figure 3 (magnitudes of events vs. time) and summarized in Table 1. It is built from the ISC-GEM, ISC, and Global CMT catalogs. The ISC-GEM instrumental catalog is updated regularly (1900–2013, Storchak *et al.*, 2015; v. 4.0 released in January 2017). This catalog results from an extensive effort to collect and digitize a new parametric earthquake bulletin. Hypocenters have been computed from the original arrival-time data using the same technique and velocity model (Di Giacomo *et al.*, 2015). Uniform procedures have been applied to determine magnitude throughout the entire catalog; surface wave M_s and short-period body wave m_b were recomputed; M_w magnitudes are derived either from the Global CMT project (Dziewonski *et al.*, 1981; Ekström *et al.*, 2012), or computed from published estimates of seismic moment or from proxy values obtained by converting the M_s and m_b magnitudes. Overall, 212 earthquakes (M_w 5.1–8.4) fall in our spatial window of interest, including five events that belong to the ISC-GEM supplement catalog (see Storchak *et al.*, 2015).

Solutions for earthquakes with lower magnitudes or earthquakes in the early instrumental period that were not included in the ISC-GEM project are retrieved from the ISC event catalog. The ISC Bulletin is the most complete source of earthquake solutions on a global scale. It reports both revised and preliminary locations using a merged dataset of arrival times provided by global, regional, and local

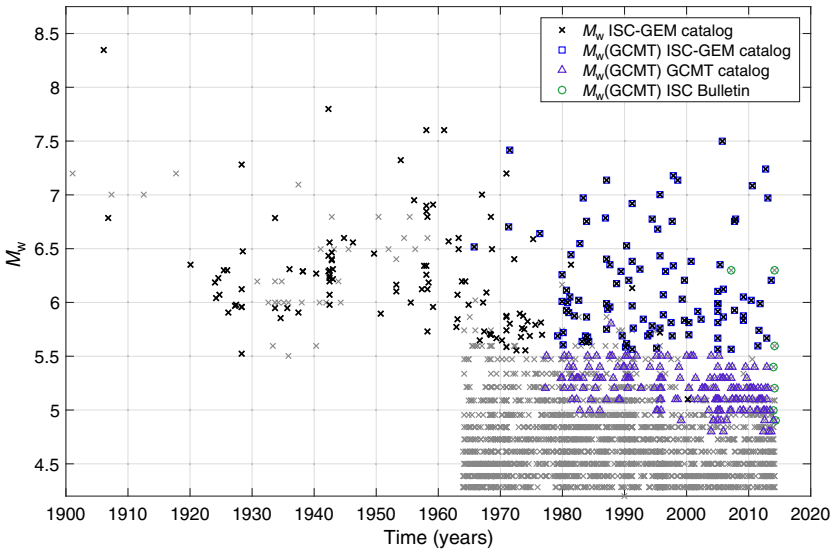

Figure 3. Final International Seismological Centre (ISC)-based earthquake catalog, built from the ISC-Global Earthquake Model (GEM), ISC, and Global Centroid Moment Tensor (GCMT) catalogs, homogenized in magnitude M_w. The color version of this figure is available only in the electronic edition.

contributing institutions. Here, we use the ISC event catalog, which provides a preferred (prime) location and the list of all magnitudes available for an event. The reviewed period extends to 2014. When available, the location calculated by the ISC is always selected as prime location. In the early instrumental period (1900–1963), there were 32 events in the ISC catalog that were not included in the ISC-GEM catalog (Fig. 3). Solutions for these events are more uncertain than ISC-GEM solutions; nonetheless they are taken into account. Of these events, 27 have a magnitude estimated by Pasadena (PAS) (Gutenberg and Richter, 1965), 1 by P&S (Pacheco and Sykes, 1992), 2 by AN2 (Abe and Noguchi, 1983), and 2 by ISC. Magnitudes in the early instrumental period are considered surrogates to the moment magnitude. From 1964 on, the list of magnitudes available can be long and a priority scheme is required. For each event, the preferred magnitude is selected from the following magnitude authors list, applying a ranking for authors and magnitude type: M_w Global CMT/HRV > M_w NEIC > m_b ISC > m_b NEIC or NEIS or United States Coast and Geodetic Survey (decreasing order of priority). Because many Global CMT M_w magnitudes are lacking in the ISC event catalog, we extracted them directly from the original Global CMT catalog (see Data and Resources). Body-wave magnitudes m_b and surface-wave magnitudes M_s are converted into M_w by applying Lolli *et al.* (2014) global equations (Fig. 4).

The 2319 earthquakes from the ISC event catalog (M_w proxy ≥ 4.2) are appended to the 212 events from the ISC-GEM catalog ($M_w \geq 5.5$, one exception with M_w 5.1, Table 1). The final ISC-based catalog contains 2531 events with $M_w \geq 4.2$ (Fig. 3). For the first half of the century (1900–1963), only magnitudes down to M_w 5.5 are reported in the catalog. Original magnitude types and authors are summarized in Table 1, showing that around 88% of all events in the final catalog are described by a magnitude m_b converted into M_w with the Lolli *et al.* (2014) equation.

Table 2
Completeness Periods per Magnitude Interval for the Three Homogenized and Declustered Earthquake Catalogs

Magnitude of Completeness	ISC-Based Catalog	NEIC-Based Catalog	BSSA2013 Catalog
4.2	1969	1973	1995
4.5	1964	1973	1963
4.8	1964	1973	1963
5.1	1964	1973	1963
5.4	1964	1971	1963
5.7	1957	1965	1963
6.0	1925	1930	1900
6.3	1925	1920	1900
6.6	1925	1920	1900
6.9	1900	1900	1900
7.2	1900	1900	1800
≥ 7.5	1900	1900	1750

BSSA2013, Beauval *et al.* (2013).

Magnitude–Frequency Distributions

The most widely used model to estimate frequencies of earthquakes in seismogenic sources is the Gutenberg–Richter model (Gutenberg and Richter, 1944). The logarithm of the number of earthquakes decreases linearly with magnitude in most source zones in Ecuador. However, depending on the available data, the Gutenberg–Richter parameters are sometimes poorly constrained and the uncertainty on the recurrence model needs to be taken into account. Even in sources with many events, the modeling of the recurrence bears significant uncertainties: uncertainties on earthquake hypocentral locations and magnitudes, the scheme established to select the best solutions, the choice of magnitude conversion equations, the identification of clustered events, the determination of completeness periods, the magnitude range and magnitude bin width used to model the recurrence, and the method selected to estimate recurrence parameters. Therefore, we decided to use three alternative earthquake catalogs, each with their own advantages and disadvantages, as a way to estimate the uncertainty on the recurrence model within the source zones. The three alternative recurrence models are included in the logic tree.

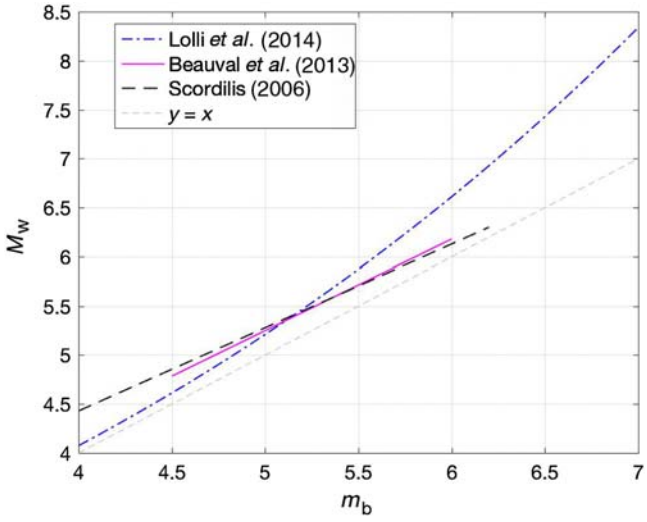

Figure 4. Magnitude conversion equations, m_b into M_w. Lolli *et al.* (2014) is used for the ISC-based and National Earthquake Information Center (NEIC)-based catalogs (see the Earthquake Catalogs section). Beauval *et al.* (2013) is used in the BSSA2013 catalog. The color version of this figure is available only in the electronic edition.

In the Fault and Background Model section, we present a set of the best-characterized crustal fault sources. For each crustal source zone that encloses a fault, maximum magnitude bounding the recurrence model is inferred from the area of the fault by applying the Leonard (2010) scaling relationship (see Tables 5 and 6, and the Fault and background Model section). In two sources, Pallatanga and El Angel, the magnitude of the largest historical event estimated from intensities (67th percentile, Beauval *et al.*, 2010) is larger than the magnitude obtained from the scaling relationship; therefore, the maximum observed magnitude is used instead. For intraslab sources, an arbitrary 0.5 degree is added to the maximum observed magnitude. The interface source zones are modeled as dipping planes. The maximum magnitudes for the segments of the interface source zones are obtained from the Strasser *et al.* (2010) scaling relationship for interface events ($M_w = a + b\log_{10}(L)$, in which $a = 4.868$ and $b = 1.392$), considering the maximum length of the segment at 50 km depth for Esmeraldas (627 km) and at 40 km depth for La Plata (181 km), Golfo de Guayaquil (134 km), and Talara (246 km). Maximum magnitudes for all sources are given in Table 3.

Table 3
Area Model, Parameters of Magnitude–Frequency Distributions, and Supplementary Information for Each Source Zone (relying on the BSSA2013 catalog)

Zone	a	b	$\lambda_{M_w \geq 4.5}$	M_0 for GR	Number of Events $\geq M_0$	M_{maxobs}	M_{max}	Depth Range
Cosanga	2.7701	0.71	0.3866	4.8	13	7.1	7.8	0–35*
Moyobamba	4.4484	0.98	1.082	4.8	28	6.9	7.7	0–35*
Cutucu	5.4443	1.17	1.436	4.5	69	7.0	7.8	0–35*
Chingual	3.0831	0.98†	0.046	4.2	3	7.4	7.6	0–35*
Napo	3.4369	0.98†	0.106	4.5	5	5.6	7.8	0–35*
Pallatanga	2.8012	0.73	0.341	4.5	18	7.6	7.9	0–35*
Quito Latacunga	2.6797	0.70	0.336	4.5	17	6.4	7.3	0–35*
Puna	3.5830	0.98†	0.149	4.5	7	5.2	7.5	0–35*
El Angel	3.4503	0.98†	0.127	4.5	9	7.2	7.7	0–35*
Yaquina Shallow	6.7516	1.39	3.012	4.8	55	6.1	6.6	0–50*
Esmeraldas	4.0002	0.81	2.341	4.8	74	8.8(8.4‡)	8.8	3–50§
La Plata	3.5598	0.80	0.915	4.5	46	6.7	8.0	3–40§
Golfo de Guaya	3.4765	0.84	0.492	4.5	25	7.5	7.8	3–40§
Talara	4.3639	0.91	1.916	4.8	53	7.1	8.2	3–40§
Loja	6.8273	1.33	6.718	4.8	130	7.2	7.7	35–100*
Morona	4.4742	0.89	2.958	4.8	84	7.3	7.8	100–130*
Puyo	5.3015	1.05	3.6	4.8	88	7.5	8.0	130–300*
Subvolcanic arc	5.0710	1.11	1.141	4.5	55	6.7	7.2	35–180*
Caldas cluster	4.7058	1.05	0.987	4.8	24	6.7	7.2	35–250*
Loreto	7.3757	1.62	1.279	4.8	20	7.5	8.0	130–180*
BGN‖	4.5245	1.09	0.428	4.8	10	6.4	7.0	0–35*
BGS‖	4.5428	1.04	0.697	4.5	36	7.2	7.5	0–35*

a- and b-values of the Gutenberg–Richter (GR) model using the BSSA2013 catalog, annual exceedance rate of M_w 4.5, minimum magnitude used in the recurrence modeling, number of events to derive the model (inside periods of completeness), maximum observed magnitude, and maximum magnitude bounding the recurrence model.

*A probability density function for the depth is built from the depths of earthquakes belonging to each source, distributing earthquakes between the minimum and maximum depths.

†b-value estimated over the whole Cordillera and coastal plain.

‡Magnitude M_w of the 1906 event estimated 8.4 in the ISC-GEM catalog (Di Giacomo *et al.*, 2015).

§The recurrence model is built from earthquakes falling inside the volume, then distributed over a dipping fault plane extending from the minimum to the maximum depth.

‖Two background sources added with respect to Yepes *et al.* (2016) crustal model.

Table 4
Parameters Used in the Probabilistic Seismic Hazard Assessment (PSHA) Calculation

Parameter	Value Used
M_{min}	M_w 5.0
Maximum distance	250 km
Truncation of σ	+4
V_{S30}	760 m/s

Minimum magnitude used for integrating the magnitude–frequency distributions, maximum source–site distance taken into account, truncation level of the Gaussian predicted by the GMM, and V_{S30} of the generic sites.

A set of recurrence parameters (a- and b-values) is obtained from each earthquake catalog, yielding three alternative areal source models. Recurrence parameters are estimated using the maximum-likelihood method of Weichert (1980), with a 0.3 magnitude interval and a minimum magnitude varying from M_w 4.2 to 4.8, depending on the source. Table 3 summarizes the values obtained from the BSSA2013 catalog. Figure 5 displays the recurrence curves modeled from the three alternative earthquake catalogs for eight example sources that contributed significantly to the hazard. For intraslab sources, all magnitude–frequency distributions except one (Loreto) are well constrained and rely on many events (55–130 events inside periods of completeness), and the three earthquake catalogs provide close recurrence curves. Recurrences obtained for Loja (35–100 km depth), Morona (100–130 km), and subvolcanic arc (35–180 km) are displayed in Figure 5. The thickness of the Morona source is only 30 km; this source presents the highest earthquake density among intraslab sources.

Magnitude–frequency distributions are rather well constrained in only five out of nine crustal sources (Cutucu, Moyobamba, Pallatanga, Cosanga, and Quito-Latacunga).

Table 5
Fault Parameters—Geologic Model

Fault	Mechanism	L (km)*	Slip Rate (mm/yr)	Maximum Depth	Dip (°)	Width	Alpha (10^{-4})†	M_{max} from A‡	M_{max} Final	b-Value§	a-Value Calculated
Chingual	SS	136	9.8	18	90	18	0.2012	7.4	7.6	0.98	4.65
Cosanga	R	189	9.0	25	40	36	0.2088	7.8	7.8	0.71	3.0
Quito	R	80	1.0	25	55	28	0.2411	7.3	7.3	0.70	1.93
Latacunga	R	48	2.1	25	45	32	0.2626	7.2	7.2	0.70	2.27
Pallatanga	SS	180	3.1	18	75	19	0.1920	7.5	7.9	0.73	2.53
Puna	SS	172	6.0	18	90	18	0.1935	7.5	7.5	0.98	4.42

SS, strike slip; R, reverse.
*Length of the fault estimated from the trace.
†Ratio of the average displacement (Dav) in the largest earthquake rupturing the fault to the fault length. Dav estimated from length L, applying Leonard (2010) scaling relationship: Dav $= 10^{0.833\times\log_{10}(L)-1.34}$ for strike-slip events, and Dav $= 10^{0.833\times\log_{10}(L)-1.30}$ for reverse events.
‡Maximum magnitude estimated from the area $A = LW$, applying Leonard (2010) scaling relationship: $M_w = \log_{10}(A) + 3.99$ for strike-slip events, and $M_w = \log_{10}(A) + 4.00$ for reverse events.
§b-values of area source zones enclosing the fault systems (in this case, based on the BSSA2013 catalog).

Table 6
Fault Parameters—Geodetic Model (No Aseismic Component)

Fault	Mechanism	L (km)*	Slip Rate (mm/yr)	Maximum Depth	Dip (°)	Width	Alpha (10^{-4})†	M_{max} from A‡	M_{max} Final	b-Value§	a-Value Calculated
Chingual	SS	136	8.1	18	90	18	0.2012	7.4	7.6	0.98	4.57
Cosanga	R	189	9.5	25	40	36	0.2088	7.8	7.8	0.71	3.02
El Angel	SS	118	2.0	18	90	18	0.2061	7.3	7.7	0.98	3.98
Quito	R	80	4.5	25	55	28	0.2411	7.3	7.3	0.70	2.59
Latacunga	R	48	1.0	25	45	32	0.2626	7.2	7.2	0.70	1.95
Pallatanga	SS	180	7.4	18	75	19	0.1920	7.5	7.9	0.73	2.91
Puna	SS	172	7.1	18	90	18	0.1935	7.5	7.5	0.98	4.50
Napo	R	151	2.5	25	30	46	0.2168	7.8	7.8	0.98	4.29

*Length of the fault estimated from the trace.
†Ratio of the average displacement (Dav) in the largest earthquake rupturing the fault to the fault length. Dav estimated from length L, applying Leonard (2010) scaling relationship: Dav $= 10^{0.833\times\log_{10}(L)-1.34}$ for strike-slip events, and Dav $= 10^{0.833\times\log_{10}(L)-1.30}$ for reverse events.
‡Maximum magnitude estimated from the area $A = LW$, applying Leonard (2010) scaling relationship: $M_w = \log_{10}(A) + 3.99$ for strike-slip events, and $M_w = \log_{10}(A) + 4.00$ for reverse events.
§b-values of area source zones enclosing the fault systems (in this case, based on the BSSA2013 catalog).

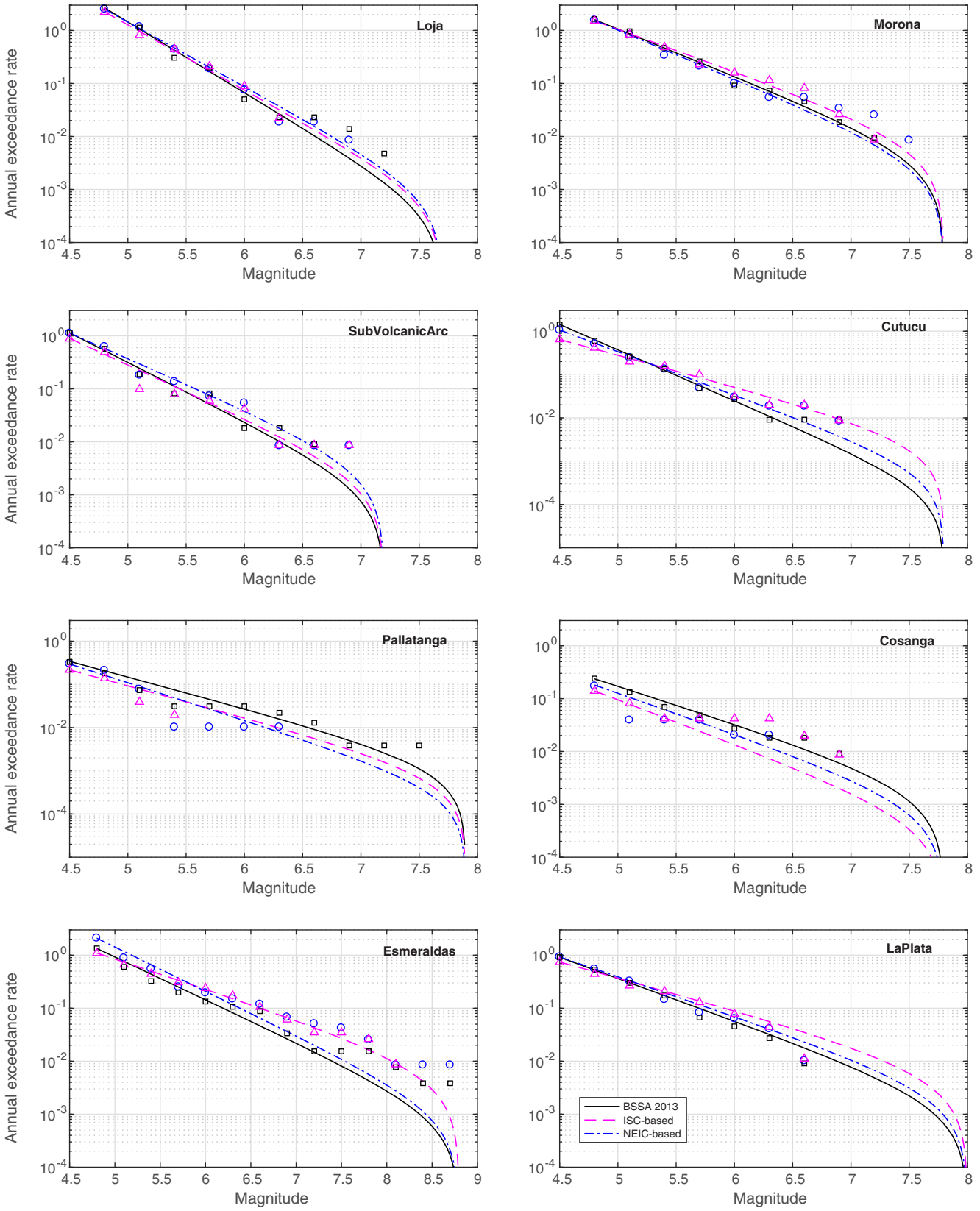

Figure 5. Truncated exponential magnitude–frequency distributions for example source zones significantly contributing to the hazard in Ecuador. Symbols: observed magnitude rates. Three alternative catalogs are used: BSSA2013 catalog (1541–2009, squares), ISC-based catalog (1900–2014, triangles), and NEIC-based catalog (1900–2017, circles). See the Earthquake Catalogs and Magnitude-Frequency Distributions sections. The color version of this figure is available only in the electronic edition.

Crustal earthquakes were extracted from the earthquake catalog using a cutoff value of 35 km (Yepes *et al.*, 2016). The models for the Cutucu (Fig. 5) and Moyobamba sources are derived from 69 ($M_w \geq 4.5$) and 28 ($M_w \geq 4.8$) events, respectively, inside completeness time periods (numbers given for the BSSA2013 catalog). The Cutucu zone is expected to significantly influence the hazard for sites in Ecuador. The influence of Moyobamba will be smaller because it is located in Peru at distances greater than 60 km from Ecuador's southeastern border. There are fewer events inside the Pallatanga, Cosanga, and Quito-Latacunga source zones, but there are still enough to derive a recurrence model (Table 3 and Fig. 5). In the four remaining source zones (Chingual, El Angel, Napo, and Puna), there are too few events to derive reliable recurrence parameters, and the model is built from the observed cumulated annual rate at the minimum magnitude considered associated with a regional *b*-value (calculated over the whole Cordillera and coastal plain area).

Magnitude–frequency distributions are rather well constrained for interface sources. In the Esmeraldas zone, the model is built from 74 events with magnitude higher or equal to M_w 4.8 inside the completeness periods (down to 50 km depth). The recurrence models inferred from the BSSA2013 and NEIC-based catalogs are similar for magnitudes larger than M_w 6.0, but the recurrence model inferred from the ISC-based catalog predicts much higher rates (Fig. 5). Recurrence parameters for La Plata are rather well constrained, estimated from magnitudes M_w 4.5 to 6.7 (maximum observed magnitude in the BSSA2013 catalog). The recurrence model is then extrapolated up to the maximum magnitude M_w 8.0 (Fig. 5). The Golfo de Guayaquil source is the less active of the interface sources with a recurrence curve established from 25 events with $M_w \geq 4.5$ (Table 3). North of −2.5° latitude, sites on the Ecuadorian coast located over the interface rupture plane are thus at short distances from the rupture plane (shortest distances 20–30 km for the coastal region between Pedernales and Esmeraldas, Fig. 1). South of −2.5° latitude, sites in Ecuador are at greater distances from the interface rupture plane.

We notice that for the crustal source Cutucu and the interface source Esmeraldas, the rates based on the ISC-based catalog are significantly larger than the rates determined from the BSSA2013 catalog for magnitudes larger than $M_w \sim 5.5$ (the opposite occurs for magnitudes lower than $M_w \sim 5.5$). One explanation might be the use of the Lolli *et al.* (2014) equation to convert m_b magnitudes into M_w in the ISC-based catalog, whereas an equation developed from data in and around Ecuador, very similar to the global Scordilis (2006) equation, was used in BSSA2013. Figure 4 displays these conversion equations. The Lolli *et al.* (2014) equation has been carefully developed on a much larger global dataset than previous equations, applying a chi-square general orthogonal regression method that accounts for measurement errors. Considering Lolli *et al.* (2014) the most reliable conversion equation, the BSSA2013 equation might overestimate M_w for magnitudes lower than $m_b \sim 5.2$ and underestimate M_w for larger m_b. As observed in these two sources, the decisions taken to homogenize an earthquake catalog can strongly impact the Gutenberg–Richter curve modeling. However, this discrepancy is only observed in some sources, thus the choice of the conversion equation might not be an unique explanation.

For each source, the three earthquake catalogs yield three recurrence models, which are considered representative of the uncertainty on the recurrence modeling. These alternative models are included in the logic tree.

Selection of Ground-Motion Models

Several GMMs must be selected from published robust models to represent the epistemic uncertainty in ground-motion prediction (Stewart *et al.*, 2015). Although the models developed for crustal events are numerous, there are fewer models predicting ground motions for subduction interface and intraslab events (Douglas and Edwards, 2016). When strong-motion recordings are available, the models that best fit the data should be selected. However, for the selection to be reliable, the accelerometric data must be well distributed over a large magnitude range (from moderate magnitudes to magnitudes close to the maximum magnitude) and a large distance range (including short distances that control the hazard). Except for earthquakes at the Esmeraldas interface, such a dataset does not yet exist for Ecuador. The strong-motion network started in 2009 with nine stations installed in the framework of the French–Ecuadorian research project Andes du Nord (ADN). At present, the national strong-motion network (Red Nacional de Acelerógrafos [RENAC]) includes more than 80 stations, progressively installed since 2011. The network is still in development, with ∼30% of the stations telemetered and the characterization of the sites undergoing.

Three robust GMMs are considered for subduction earthquakes: the global model Abrahamson *et al.* (2016; hereafter, Aetal2016), the Chilean model Montalva *et al.* (2017; hereafter, Metal2017), and the Japanese model Zhao *et al.* (2006; hereafter, Zetal2006). The Aetal2016 model is intended to replace older global GMMs. The Metal2017 median model is based on Chilean data, using the same functional form as the Aetal2016 model. The Aetal2016 and Zetal2006 models were ranked among the best-fitting models in several studies comparing predictions with recordings from South America (e.g., Arango *et al.*, 2012; Beauval, Cotton, *et al.*, 2012). Beauval *et al.* (2017) compared the ground motions from the 2016 M_w 7.8 Pedernales megathrust earthquake and its two largest aftershocks (M_w 6.7 and 6.9) to the predictions of these three GMMs. The comparison between observed and predicted ground motions showed that the three models properly predict the amplitudes attenuation in the fore-arc domain. The analysis also demonstrated that the high-frequency attenu-

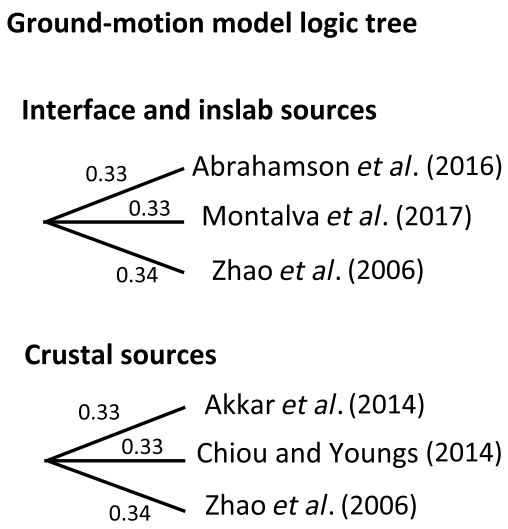

Figure 6. Ground-motion logic tree.

ation is stronger for sites located in the back-arc region with respect to sites located in the fore-arc region, an effect that only the Aetal2016 model takes into account. However, the contribution of interface subduction sources is negligible for rock sites in the arc and back-arc region in Ecuador (for the PGA and return periods ≥ 475 yrs, as will be shown in the Hazard Estimates for Area Source Models section), so the three models are included in the ground-motion logic tree (Fig. 6). The Pedernales earthquake produced a large sequence of aftershocks, with eight events having magnitude equal to or higher than M_w 6.0. Candidate GMMs should be tested against this dataset by applying quantitative methods to potentially refine the selection (e.g., Scherbaum *et al.*, 2009; Beauval, Tasan, *et al.*, 2012). Zhao *et al.* (2016) published an update of the 2006 interface model (as well as crustal and inslab models), but we need to test it against observations before using it.

For intraslab sources, the same three models are selected. Intraslab volumes are defined down to 300 km depth (Table 3). Aetal2016 recommend a depth limit of 120 km for intraslab events when applying the model. The Zetal2006 and Metal2017 databases include intraslab events with focal depths shallower than 125 and 180 km, respectively. Aetal2016 and Zetal2006 must be extrapolated at depths larger than 120–130 km—four sources include such large depths, including the very active Puyo source (130–300 km, Yepes *et al.*, 2016). We calculated the hazard with and without these sources, and we observed that their contribution is not significant. Historical intraslab earthquakes in Ecuador have shown that intensities up to VI–VII are observed at the coast for large deep intraslab earthquakes (e.g., 1971 M_w 7.4, 120 km depth, located in the Morona source), whereas much lower intensities are observed for sites above the hypocenter. This effect, related to the lower attenuation of waves inside the slab (high-Q zone, Fukushima, 1997), is not accounted for in current GMMs.

Because the RENAC database does not include enough crustal events of significant magnitude to perform a meaningful test against GMM candidates, the selection of active crustal GMMs take inspiration from the outputs of the South America Risk Assessment (SARA) GMM working group (Drouet *et al.*, 2017). GMMs were tested against a homogeneous strong-motion database gathering data from Colombia, Chile, Ecuador, and Venezuela. The dataset from Ecuador includes only small events with magnitudes between M_w 4.0 and 5.0. The log-likelihood method was applied to rank the models according to their fit to the data (Scherbaum *et al.*, 2009). Obtained log-likelihood values (see Scherbaum *et al.*, 2009) are quite high for all models (2.8–3.7 for the PGA and 0.2 s, table 2 in Drouet *et al.*, 2017), indicating that none of the models are able to satisfactorily predict the South American dataset. Drouet *et al.* (2017) note that the observed variability is greater than the GMMs prediction, suggesting that more efforts are needed to improve the database, particularly the estimation of V_{S30} values. According to Garcia *et al.* (2017), the three models finally selected for SARA hazard calculations are Akkar *et al.* (2014), Bindi *et al.* (2014), and Boore *et al.* (2014). For hazard calculations in Ecuador, we decided to select Akkar *et al.* (2014), which was established from Mediterranean and Middle East strong motions (Reference Database for Seismic Ground-Motion in Europe [RESORCE] data bank). From the Next Generation Attenuation-West2 models, developed from western United States and international data, the Chiou and Youngs (2014) model is preferred over the Boore *et al.* (2014) model because it accounts for some factors that affect earthquake ground motions (e.g., hanging wall and rupture directivity). Lastly, rather than selecting a second model based on the RESORCE data bank (Bindi *et al.*, 2014), the Zhao *et al.* (2006) Japanese model is selected. The equation is based on data recorded in a tectonic environment close to the Ecuadorian Cordillera hosting many volcanoes. Tested against diverse strong-motion datasets, this equation proved to be robust and stable over the full frequency range (e.g., Beauval, Tasan, *et al.*, 2012; Delavaud *et al.*, 2012). The V_{S30} values must be mapped to site classes following table 2 in Zhao *et al.* (2006). The final GMM logic tree is described in Figure 6.

In this study, probabilistic seismic hazard calculations are performed with the OpenQuake engine (Pagani, Monelli, Weatherhill, Danciu, *et al.*, 2014; GEM, 2017). OpenQuake represents the seismogenic source as a finite rupture. For an area source, a mesh is created over the area and virtual ruptures are generated at each node. The scaling of the rupture depends on the scaling relation selected and the orientation on a set of parameters (nodal plane distribution, hypocentral depth distribution, and upper and lower seismogenic depths; see Monelli *et al.*, 2014). As for fault sources, using the simple fault typology (here for crustal faults) or the complex fault typology (for interface segments), the ruptures are distributed along the fault surface. A mesh is created across the

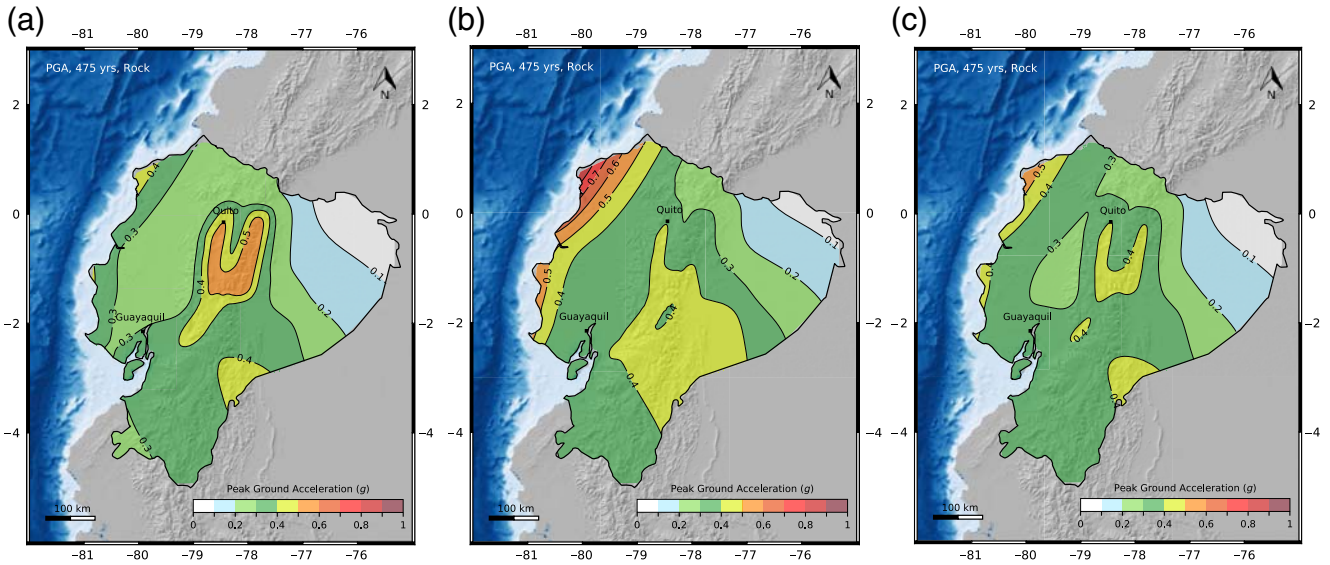

Figure 7. Mean hazard map at 475-yr return period, for peak ground acceleration (PGA) (V_{S30} 760 m/s), using one area source model and the full ground-motion model (GMM) logic tree. Area model based on (a) the BSSA2013 earthquake catalog (50% weight in the final logic tree); (b) the ISC-based earthquake catalog (40% weight); and (c) the NEIC-based earthquake catalog (10% weight). The color version of this figure is available only in the electronic edition.

fault surface and individual ruptures are represented by a subset of nodes within that mesh. Rupture distance is determined from the shortest distance between the target site and the individual rupture. Joyner and Boore distance is determined from the shortest distance between the target site and the surface projection of the fault. More details can be found in the OpenQuake-engine Hazard Book (Pagani, Monelli, Weatherill, and Garcia, 2014).

Hazard Estimates for Area Source Models

Three hazard maps corresponding to the three alternative area source models are calculated for the PGA and for the return period 475 yrs. Results based on recurrence parameters obtained from the BSSA2013, ISC-based, and NEIC-based catalogs are displayed respectively in Figure 7a–c. Parameters used to perform PSHA calculations throughout the article are indicated in Table 4. These maps are mean hazard maps, because the full ground-motion prediction logic tree is considered. South of latitude −2°, acceleration values vary in a 0.1g interval from one model to the other, with the highest hazard value 0.4–0.5g from the ISC-based model (highest recurrence rates for the Cutucu source zone). Inside the Quito source zone accelerations also differ within a 0.1g interval, with the highest accelerations (0.5–0.6g) obtained using the BSSA2013 model. The difference in acceleration is larger for sites located inside the Cosanga source zone; the highest accelerations are obtained using the BSSA2013 model, in agreement with the recurrence models obtained in this source zone (Fig. 5). The most striking difference is obtained for sites at the coast north of latitude −1°, located above the Esmeraldas source rupture plane. The recurrence model determined from the ISC-based catalog leads to much higher PGA values (0.5–1.0g) than the model that relies on the BSSA2013 catalog (0.3–0.5g) or on the NEIC-based catalog (0.3–0.6g).

The mean hazard map that relies on the three alternative area models with associated weights, combined with the full GMM logic tree, is displayed in Figure 8a. At 475 yrs, and PGA, accelerations are higher than 0.4g at sites on the coast, with maximum values around 0.6–0.7g at latitudes around +0.7°. In the Cordillera, values vary between 0.2g and 0.5g, with the highest hazard for sites inside the Quito-Latacunga, Cosanga, Pallatanga, and Cutucu source zones (see Fig. 1 for names of source zones). In addition, to identify which sources control the hazard, accelerations at 475-yr return period resulting from interface sources only, crustal sources only, and intraslab sources only are determined (Fig. 8b,d). Each mean hazard map is based on the three alternative source models (with associated weights) and the full GMM logic tree. For sites located on the coast, the interface-dipping planes fully control the hazard. For sites located inside the Cordillera, located north of −2°, contributions come mainly from shallow crustal sources, whereas for sites located south of −2°, contributions come both from intraslab and crustal sources.

The area model exhibits low hazard levels in three crustal sources in which late Holocene active faulting has been evidenced (sources El Angel, Chingual, and Puna). The El Angel source is characterized by low seismicity levels in the instrumental period, although a destructive earthquake occurred in 1868 with a magnitude M_w 7.2 estimated from intensity observations (7.1–7.7 within 67% confidence inter-

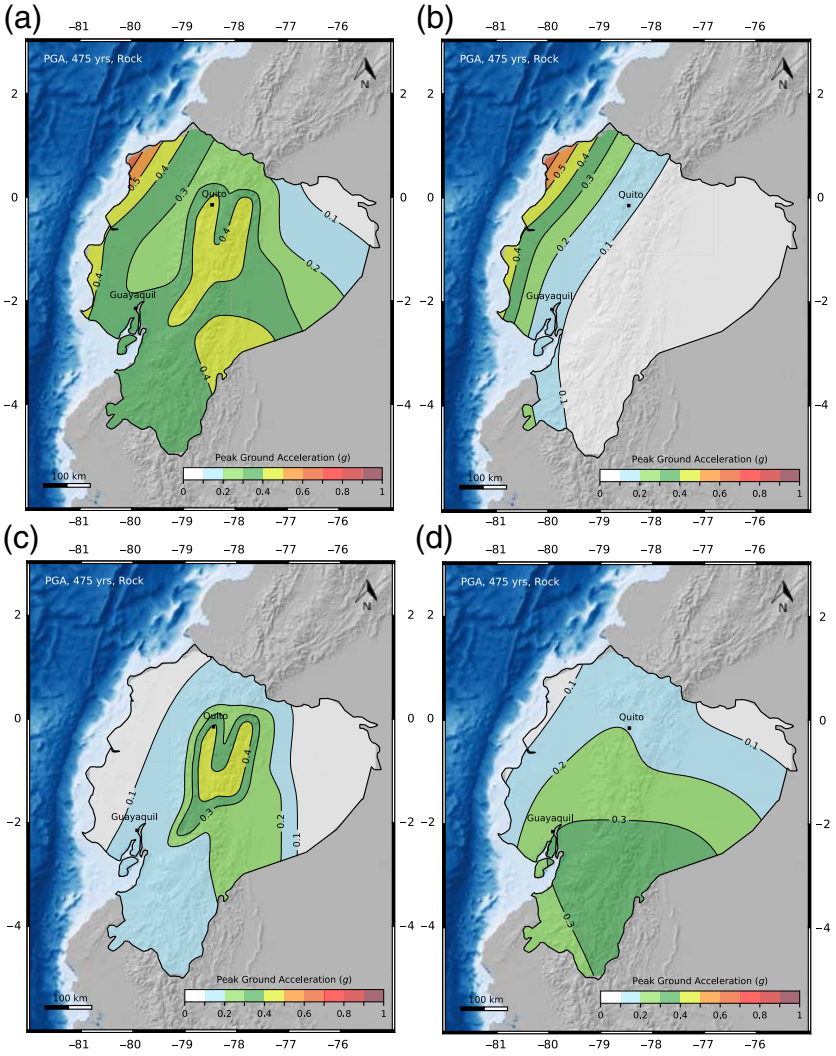

Figure 8. Hazard maps at 475-yr return period for PGA (V_{S30} 760 m/s). (a) Mean obtained from the three alternative area source models (and associated weights) and the full GMM logic tree; (b) same calculation considering only interface source zones; (c) considering only crustal sources; and (d) considering only intraslab sources. The color version of this figure is available only in the electronic edition.

val, Beauval *et al.*, 2010). The seismicity level is also low in the Chingual source zone, although in 1834 a strong earthquake destroyed Sibundoy in the northern edge of the zone (M_w 7.2–7.6, Beauval *et al.*, 2013). Various tectonic and geodetic studies have demonstrated the activity of the El Angel and Chingual fault systems (see Yepes *et al.*, 2016). Because these faults represent a significant threat to the dense population living in the Andean Cordillera, they must be accounted for in the seismic hazard assessment. In the Puna source zone, there is no known historical earthquake, but the activity of the Puna fault system has been demonstrated, with geologic slip rates up to 5.5–6.6 mm/yr (Dumont *et al.*, 2005). A slightly higher value of 7 mm/yr was found by deriving the relative motion between the North Andean and Inca slivers (Nocquet *et al.*, 2014). A fault model is therefore developed to integrate the recent geodetic and active tectonics results.

Fault and Background Model

Here, we describe how we developed a fault model with earthquake recurrences inferred from geologic and/or geodetic slip rates. Because knowledge about these crustal faults is still incomplete, strong hypotheses are necessary to propose fault-plane geometries and evaluate the fault capacity to produce earthquakes. However, the fault-source model offers the advantage of including existing information about active faults, which is not integrated in the area source model. Interface and in-slab sources remain unchanged.

Defining the Set of Active Faults

Along the Ecuadorian margin, oblique subduction induces lithospheric deformation of the overriding continental plate. Active continental deformation is presently localized along a major fault system, connecting several fault segments from the Gulf of Guayaquil to the eastern Andean Cordillera. The crustal deformation is concentrated along the Chingual-Cosanga-Pallatanga-Puna (CCPP) fault system, the Quito-Latacunga fault system, the Eastern Subandean belt, and the El Angel fault system (figs. 1 and 7 in Yepes *et al.*, 2016; Alvarado *et al.*, 2014, 2016; Baize *et al.*, 2015). The CCPP can be considered a continental microplate boundary because it accommodates around 8–10 mm/yr of relative motion between the NAS (Fig. 9) and South American plate (SOAM; Nocquet *et al.*, 2014). Its segmentation comprises northeast-striking right-lateral transpressional faults from the Gulf of Guayaquil into the Andean Cordillera (Puna and Pallatanga), with continuation along the north–south-striking transpressive faults in the eastern Andes (Cosanga) and pure strike-slip right-lateral faults further north (Chingual). In northern Ecuador, west of the CCPP boundary, the north-northeast–south-southwest fault system of El Angel comprises a series of right-lateral strike-slip faults and probably represents the southern prolongation of the major Romeral-Cauca-Patia fault system described in Colombia (Ego *et al.*, 1996; Taboada *et al.*, 2000; Yepes *et al.*, 2016). Furthermore, east of the NAS, shortening across the active Andean back-arc takes place along the eastern sub-Andean thrust-and-fold belts (Ego *et al.*, 1995; Bès de Berc *et al.*, 2005; Alvarado *et al.*, 2016).

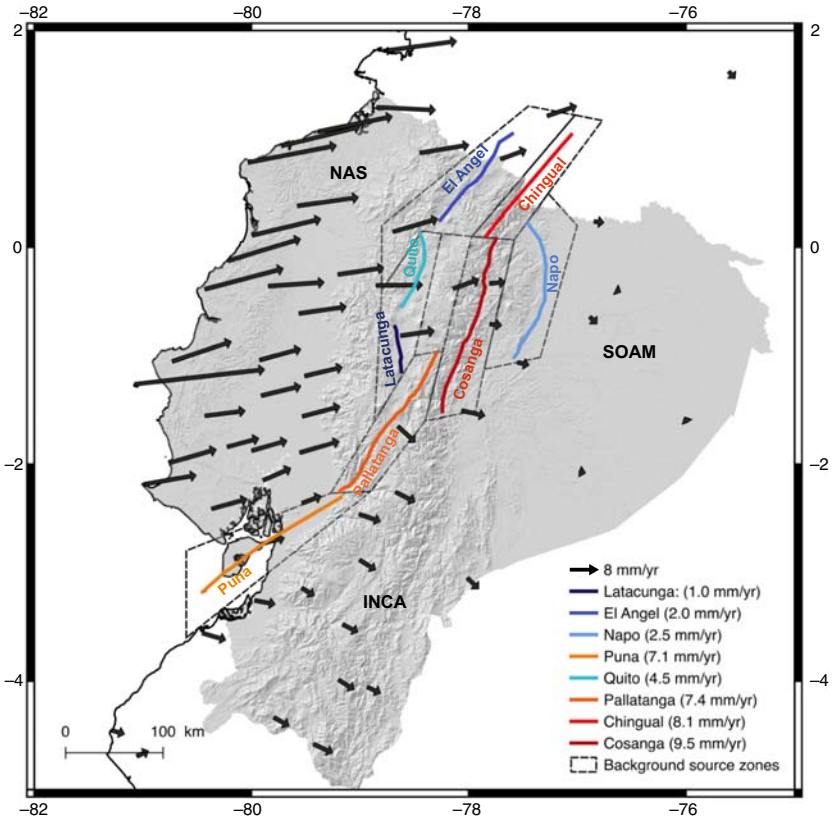

Figure 9. Global Positioning System velocity field and main faults accounted for in the probabilistic seismic hazard calculations. The slip rates estimated for each fault are indicated. Area sources enclosing faults are used as background sources (off-fault seismicity). NAS, North Andean Sliver; SOAM, South American plate; INCA, Inca sliver. The color version of this figure is available only in the electronic edition.

A set of eight crustal fault sources is defined (Fig. 9, Tables 5 and 6). Many fault segments are left aside, with respect to the active fault map (Neotec database, see Data and Resources; Audin *et al.*, 2014), because only the best-characterized segments can be included in the model. The eight fault sources have been defined by analyzing geologic data, earthquake epicenters, focal mechanisms, and GPS results. Geologic slip rates are available for six out of the eight fault sources. For the Chingual fault, Tibaldi *et al.* (2007) estimated slip rates from 7.7 to 11.9 mm/yr based on several late Pleistocene deposits displaced by various branches of the fault. They also estimated Holocene slip rates of 4.3 ± 2.2 mm/yr for the north–south reverse faults south of Chingual fault, which we considered to be part of the Cosanga transpressive fault system (northern section, Yepes *et al.*, 2016). At the southern end of the Cosanga system, Bès de Berc *et al.* (2005) report uplifting velocities of up to 9–10 mm/yr during the Holocene in the upper Pastaza valley by comparing the river incision rates with the fold-and-thrust fault uplift rates located further east. The Quito and Latacunga segments accommodate crustal east–west shortening at rates ranging from 1 to 2.1 mm/yr, respectively (Lavenu *et al.*, 1995; Ego and Sebrier, 1996). Based on paleoseismological trenching along the southern section of the Pallatanga fault, Baize *et al.* (2015) estimated an average slip rate of ∼2.5 mm/yr during the Holocene. Winter *et al.* (1993), from detailed topographic leveling, showed that moraine displacements yield a mean Holocene slip rate of 2.9–4.6 mm/yr in this area. For the Puna segment, Dumont *et al.* (2005) calculated a minimum mean slip rate of 5–7 mm/yr from one particular location on the Puna island during late Pleistocene. Average values of the above-mentioned studies are used in the hazard calculations (Table 5).

In regard to the faults dip, Tibaldi *et al.* (2007) extensively verified in the field the vertical nature of the northeast–southwest right-lateral strike-slip Chingual fault system. The northern section of the Cosanga fault system shows reverse faults dipping ∼70° to the east (Tibaldi *et al.*, 2007), consistent with the nodal planes derived from the 1987 M_w 6.4 (73°) and 7.1 (64°) earthquakes focal mechanisms (Global CMT catalog). At the southern end of the Cosanga system, Bès de Berc *et al.* (2005) report that the sub-Andean uplift is likely related to the presence of a regional scale low-angle westerly dipping thrust ramp underlying the sub-Andean folds belt. Three focal mechanisms in 1987 associated with the Cosanga faults show nodal plane dips around 40° to the west (Global CMT catalog). It is conceivable that this transpressive section of the microblock boundary evolves from almost vertical at the transition from the transcurrent Chingual system to the north to more gently dipping as the fault strike becomes more orthogonal to the regional compressive stresses to the south.

For the reverse Quito fault, microseismicity reveals a 55° dipping plane to the west (Alvarado *et al.*, 2014), which is corroborated by nodal planes derived from the 1990 M_w 5.3 (55°) and 2014 M_w 5.1 focal mechanisms (44°, Global CMT catalog). The Latacunga system shows divergently dipping faults dipping 70°–80° to the west along the western side of the Interandean Valley and to the east along the eastern side (Fiorini and Tibaldi, 2012). Representative focal mechanisms for these faults are 1976 M_w 5.7 (71°, Ego *et al.*, 1996) and 1996 M_w 5.9 (69°, Global CMT catalog). Using the 1996 NEIC focal mechanism solution to constrain the initial parameters, Fiorini and Tibaldi (2012) modeled the fold that results from this blind thrust. The preferred result showed a gently dipping fault plane (28°) to the west. Blind thrusts tend to align vertically as they get closer to the surface because of development of folds or secondary shallower faults. The right-lateral strike-slip Pallatanga faults strike

N30°E and dip ~75° to the west, as Winter *et al.* (1993) found by modeling the fault trace intersection with the topography. The Puna segment also shows a right-lateral strike-slip movement with a positive flower structure identified by Dumont *et al.* (2005) at the Puna and Santa Clara islands. This suggests a near-vertical structure at depth. The average dip values attributed to the set of simplified faults are reported in Tables 5 and 6.

For the hazard calculations, we assume that an earthquake can break over the entire area of the fault. Lengths are defined from the segmentation based on the surface fault trace and we use a maximum depth of 18 km for strike-slip faults and 25 km for thrusts. These depths are based on the analysis of the hypocentral depth distribution of earthquakes in Ecuador (Yepes *et al.*, 2016), estimates of fault widths in existing global databases (e.g., Leonard, 2010), and estimates of locking depths from geodesy and seismology along well-known faults (e.g., Smith-Konter *et al.*, 2011). Fault widths are inferred from the maximum depth and dip values associated with each fault (Tables 5 and 6). Maximum magnitudes are then determined from the resulting area, applying the Leonard (2010) scaling relationship. The depth and width assumption has a major impact on the calculated hazard, because in addition to the length, the width also contributes to define the rupture area and hence the annual seismic moment rate to be released at the fault.

Geodetic Slip Rates

The GPS horizontal velocity field of 53 sites presented in Nocquet *et al.* (2014) is used to determine the slip rate along the eight simplified faults. In a first approach, the Euler poles for the NAS and Inca Sliver (Nocquet *et al.*, 2014) are used to calculate the relative velocity along the fault delimiting their boundaries. In this case, the fault portion is assumed to accommodate all the relative motion between the two adjacent blocks. Slip rates for the Puna and Pallatanga (Inca sliver/NAS boundary) and Cosanga and Chingual segments (NAS/SOAM boundary) are determined using this approach. As an alternative method, we also use the relative horizontal velocities between pairs of GPS located on either side of the fault, far enough (~30 km) from the fault trace so that the elastic contribution from the locked portion of the faults remains small. Slip rates can thus be estimated for inter-Andean and sub-Andean faults for which no block model has been proposed yet. We also carefully checked our selection of GPS stations so that the effects of neighboring crustal faults and of subduction interface are negligible. These slip rates potentially account for internal deformation within the North Andean and Inca blocks. For the faults forming the CCPP corridor, a weighted mean value from slip rates obtained using both approaches has been used for the subsequent fault model.

Only the best-characterized fault sources are considered; thus all motion is assumed to take place along these faults. This is a strong assumption, because the deformation might be distributed over a broader area and secondary faults (e.g., Aktug *et al.*, 2009). A second issue is that, given the density of available GPS sites for continental deformation monitoring, no locking depth or coupling coefficient is available for crustal faults in Ecuador, except for Quito (Alvarado *et al.*, 2014). To account for this lack of information in our PSHA calculation, we considered two alternative cases: one calculation is made assuming faults locked over the entire seismogenic thickness and another is made with an aseismic deformation component arbitrarily fixed to 50% of the total slip rate.

Obtained geodetic slip rates are close to geologically determined slip rates for some faults (Chingual, Latacunga, Puna, and Cosanga), while they significantly disagree at some others (Pallatanga and Quito). Similar discrepancies have been found worldwide (e.g., Polonia *et al.*, 2004) and are most likely due to local variations of coupling during the earthquake cycles (e.g., Chuang and Johnson, 2011). Another simple explanation relies on the fact that geodetic models assume all relative motion to be accommodated by a single idealized fault. We also recognize that our knowledge of active faults in some areas is incomplete. Figuring out which value is most relevant for PSHA is uncertain. Next, we show some sensitivity results using different slip-rate estimates.

Hazard Estimates Based on the Fault and Background Source Model

Assuming deformation remains steady in time, the earthquake recurrence model for a fault is inferred from the average slip rate following the same methodology as Woessner *et al.* (2015; European fault model) and Beauval *et al.* (2014; Quito fault). Ignoring aseismic creep, the annual total seismic moment rate on the fault is estimated as $\dot{M}_0 = \mu SA$, in which S is the slip rate per year, μ is the shear modulus (taken as 3×10^{11} dyn/cm^2), and A is the rupture area. Assuming 50% of creep, only half of $\dot{M}_0$ is then available to generate earthquakes. A recurrence model is required to distribute the seismic moment rate that will be released on the fault through earthquakes of various magnitudes. The Anderson and Luco (1983) exponential function is selected, constrained by the slip rate, a b-value, and the maximum magnitude on the fault (for more details, see Beauval *et al.*, 2014). For each fault segment, the b-value has been estimated from the earthquake catalog in the source zone enclosing the fault. The a-values estimated for each fault are reported in Tables 5 and 6. For each fault, a magnitude –frequency distribution is established. Magnitudes larger than or equal to M_w 6.0 are distributed on the fault, whereas magnitudes lower than M_w 6.0 are distributed inside the source zone enclosing the fault as background seismicity. The fault is assumed to be the only structure in the area able to host large magnitudes. To complete the model, areas without faults remain unchanged with respect to the area model, as well as interface and inslab sources.

The probabilistic seismic hazard calculation is performed with the full ground-motion prediction logic tree.

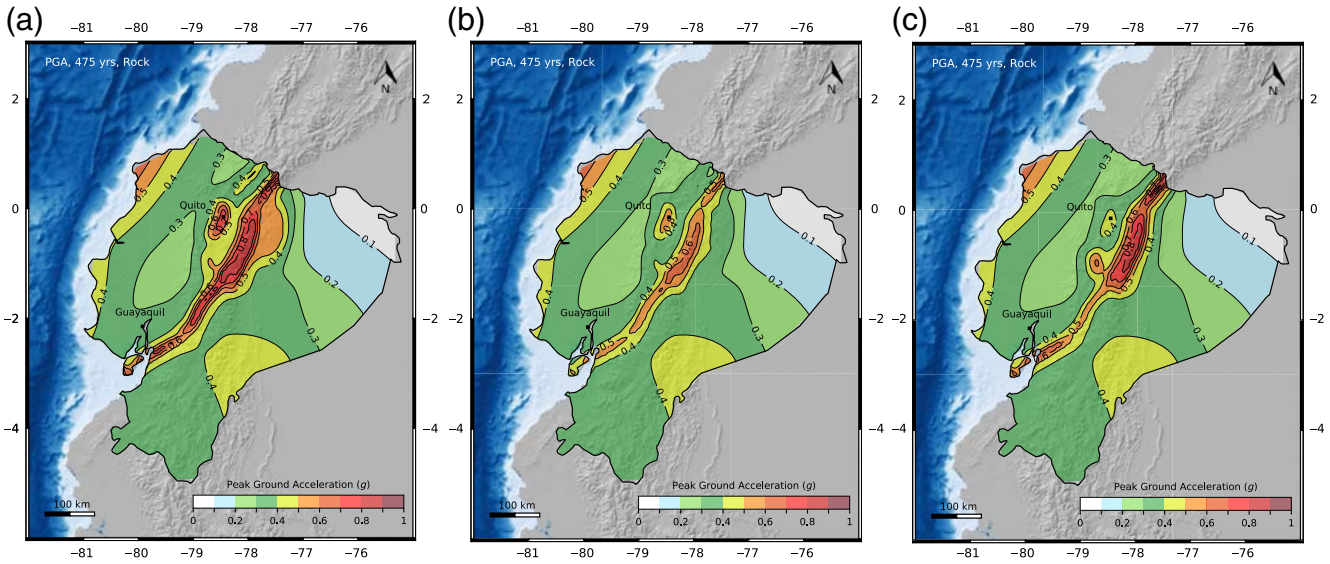

Figure 10. Mean hazard maps based on the fault and background source models, at the PGA, 475-yr return period (V_{S30} 760 m/s). Earthquake recurrence source model relying on (a) the geodetic slip rates without creep; (b) the geodetic slip rate with 50% creep; and (c) the geologic slip rate. Parameters of faults are reported in Tables 5 and 6. Exploration of the three branches corresponding to three alternative earthquake catalogs (*b*-values of the fault model; areas without faults), and full GMM logic tree (Fig. 6). The color version of this figure is available only in the electronic edition.

At 475-yr return period and for PGA, the source model based on geodetic slip rates (no aseismic component) yield accelerations higher than or equal to 0.6*g* for sites located along the CCPP fault sources (slip rates from 7.1 to 9.5 mm/yr, Table 6), as well as along the Quito fault source (4.5 mm/yr). The largest hazard values ($\geq 0.8g$) are obtained for sites right above the Cosanga thrust fault plane, as well as for those close to the Chingual strike-slip fault source (Fig. 10a). Lower values (0.4–0.6*g*) are obtained for sites above the Napo (2.5 mm/yr) and Latacunga (1.0 mm/yr) fault planes and along the El Angel strike-slip fault source (2.0 mm/yr). Arbitrarily considering 50% of aseismic deformation, the hazard obtained is much lower (Fig. 10b). For sites along the CCPP fault sources, and along the Quito fault source, accelerations are between 0.5*g* and 0.6*g*; whereas for sites along the El Angel, Latacunga, and Napo fault sources, accelerations are between 0.3*g* and 0.4*g*. Moreover, hazard maps are calculated considering geologic slip rates on the six faults where they are available (Table 5 and Fig. 10c). For sites along fault sources where geologic slip rates are close to estimated geodetic slip rates, obtained hazard values are comparable: Chingual, Cosanga, Puna (PGA > 0.6*g*). For the Quito fault source, the geologic slip rate (1 mm/yr) is much lower than the geodetic slip rate (4.5 mm/yr) and lower values are obtained (0.4*g*–0.5*g*). The opposite is observed for sites along the Latacunga fault source with values between 0.4*g* and 0.6*g* based on the geologic slip rate (2.1 mm/yr).

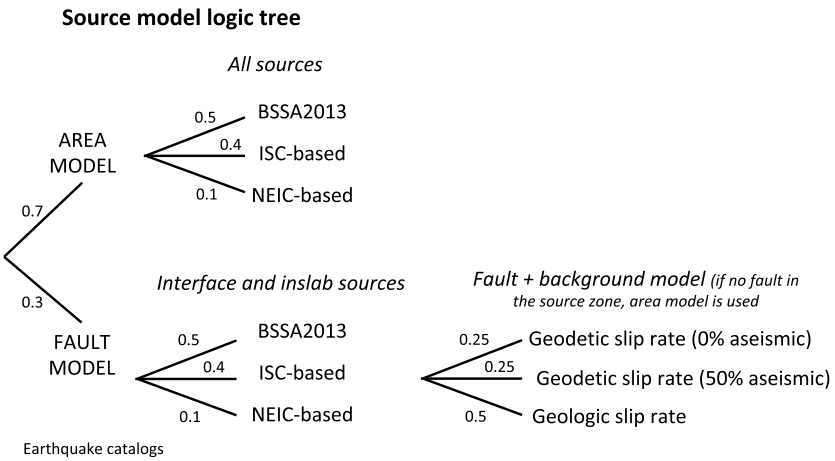

Figure 11. Source model logic tree; the combination of the branches leads to 12 alternative source models.

Complete Logic Tree

An area source model was developed in which magnitude–frequency distributions are based on three different earthquake catalogs. This area model is rather well constrained in most sources, except in four out of nine crustal sources in which regional *b*-values must be applied. A fault model is developed to take advantage of available geologic and geodetic slip rates estimated for the main crustal faults.

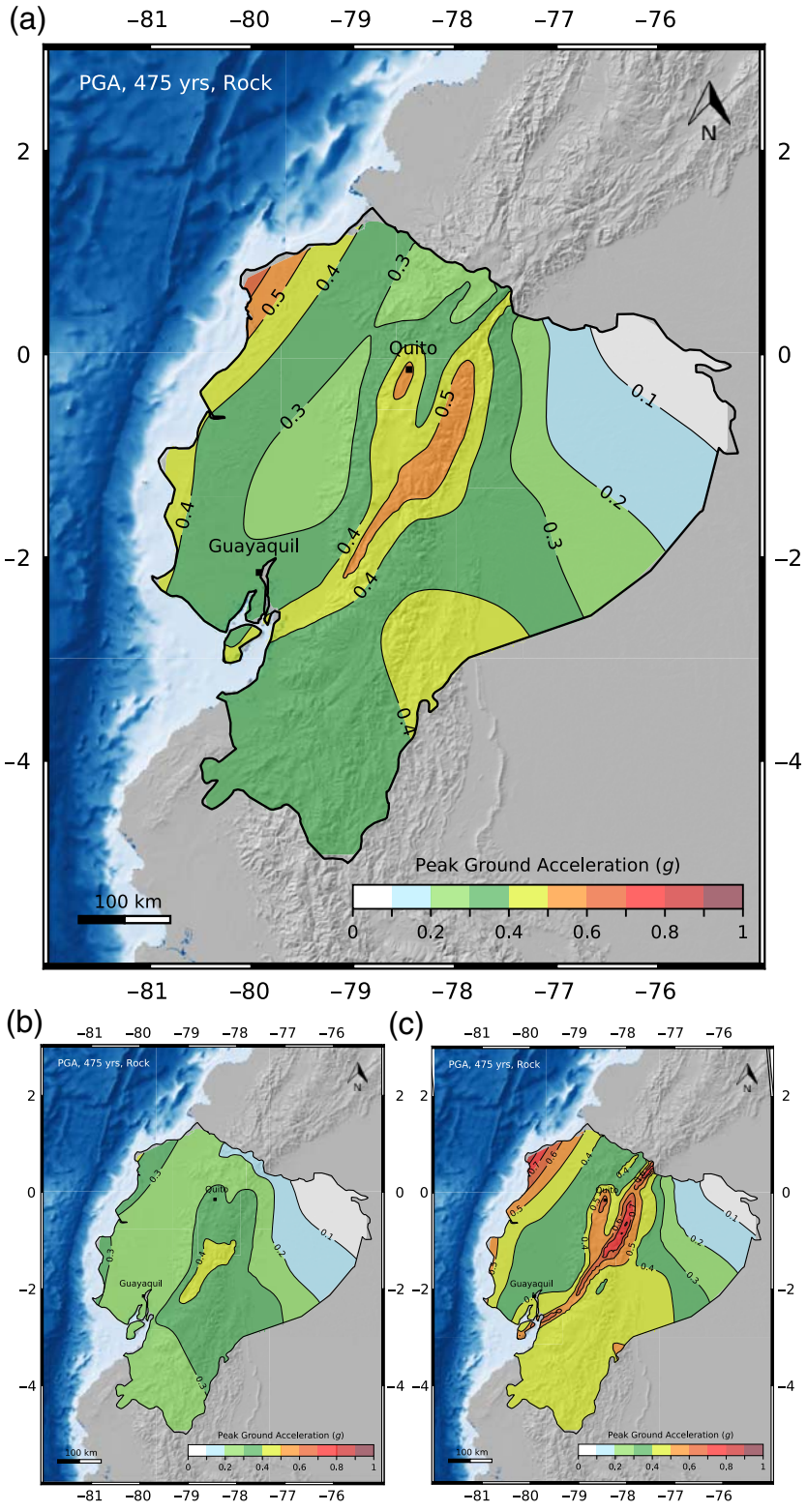

Figure 12. (a) Mean hazard map at the PGA, 475-yr return period (V_{S30} 760 m/s), from the complete logic tree, combining the source model logic tree (Fig. 11) and the ground-motion prediction logic tree (Fig. 6), as well as hazard maps corresponding to (b) the 16th and (c) 84th percentiles. The color version of this figure is available only in the electronic edition.

The area and fault models constitute two alternative source models to populate the logic tree. The fault model relies on several strong hypotheses, such as the assumption that the main structures accommodate all the measured or modeled deformation, or assumptions about the percentage of aseismic slip. Therefore, in the final logic tree more weight is given on the area model (70%) than on the fault model (30%). The scheme detailing the final source logic tree is displayed in Figure 11. Combining the source model (12 alternative models) and the GMM (3 alternative models per source type), the final logic tree is made of 324 different combinations ($12 \times 3 \times 3 \times 3$).

For simplicity and to limit the number of figures, results are shown for PGA and for the return period 475 yrs, considering a generic site with V_{S30} 760 m/s. The final mean hazard map is displayed in Figure 12, together with the maps corresponding to the 16th and 84th percentiles. Comparing the final mean values with the mean area model (Fig. 8a), including the crustal fault model in the calculation has consequences for all sites located along the CCPP corridor, as well as for sites above the Quito thrust fault plane (0.1–0.2g increase). The uncertainty on the hazard estimates is significant. Considering the hazard map corresponding to the 16th percentile, most of the country presents PGAs lower than 0.4g. Considering the 84th percentile, all sites on the coast and in the Cordillera present PGAs higher than 0.4g, reaching maximum values around 0.8g on the coast and 0.7g in the Cordillera. The uncertainty obtained is not a surprise, keeping in mind the differences in hazard obtained from different earthquake catalogs (Fig. 7), as well as the differences obtained if choosing a fault model rather than an area model (Fig. 10a–c with respect to Fig. 8a). The difference between the 16th and 84th percentile maps is displayed in Figure 13, showing that uncertainty on hazard estimates is high for sites along the northern coast (above −1°, up to 0.4–0.5g difference), and inside the Puna, Cosanga, and Chingual source zones. The largest uncertainty is found for sites inside the Chingual source zone (0.6g difference at maximum between the 16th and 84th percentiles).

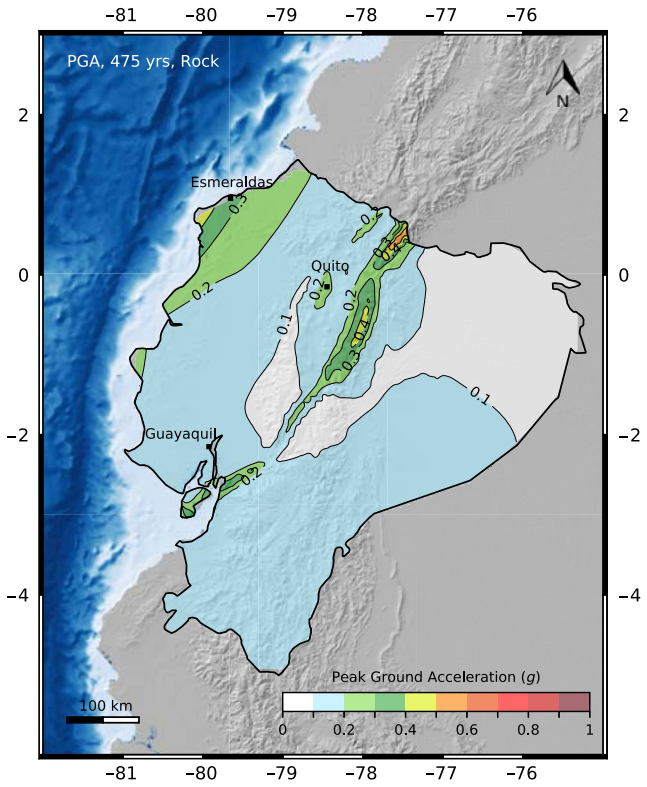

Figure 13. Uncertainty on the PGA at 475-yr return period: difference between accelerations corresponding to 84th and 16th percentiles (Fig. 12b,c). Percentiles are obtained exploring the complete logic tree (source model and ground-motion logic trees). The color version of this figure is available only in the electronic edition.

The uncertainty on the source model is responsible for a large part of the uncertainties on the final hazard estimate. The ground-motion prediction component also carries significant uncertainties. Figure 14 displayed the three hazard maps obtained by exploring the full source logic tree (Fig. 11) but fixing the GMM used for each source type. From one map to another, the models for predicting the ground motions produced by interface events and crustal events are modified. For the PGA at 475-yr return period, the Metal2017 model leads to higher hazard values for the coast than the Aetal2016 and Zetal2006 models (around $0.2g$ difference). Applying the Akkar *et al.* (2014) model rather than the Chiou and Youngs (2014) model leads to increased hazard estimates for sites in the Cordillera (around $+0.1g$).

To assess the respective contribution of the source model uncertainty and GMM uncertainty on the overall uncertainty, the hazard is calculated exploring only the source model logic tree (fixing the GMMs used), then exploring only the ground-motion logic tree (fixing the source model used). Results are displayed for three important cities in Ecuador (Fig. 15): the capital Quito, the largest city in the country Guayaquil, and Esmeraldas city, which plays a key role in the oil business. Results show that the component controlling the overall uncertainty depends on the site: in Quito and Esmeraldas, the uncertainty related to the source model is higher (or much higher) than the uncertainty related to the GMM, whereas in Guayaquil the opposite is observed.

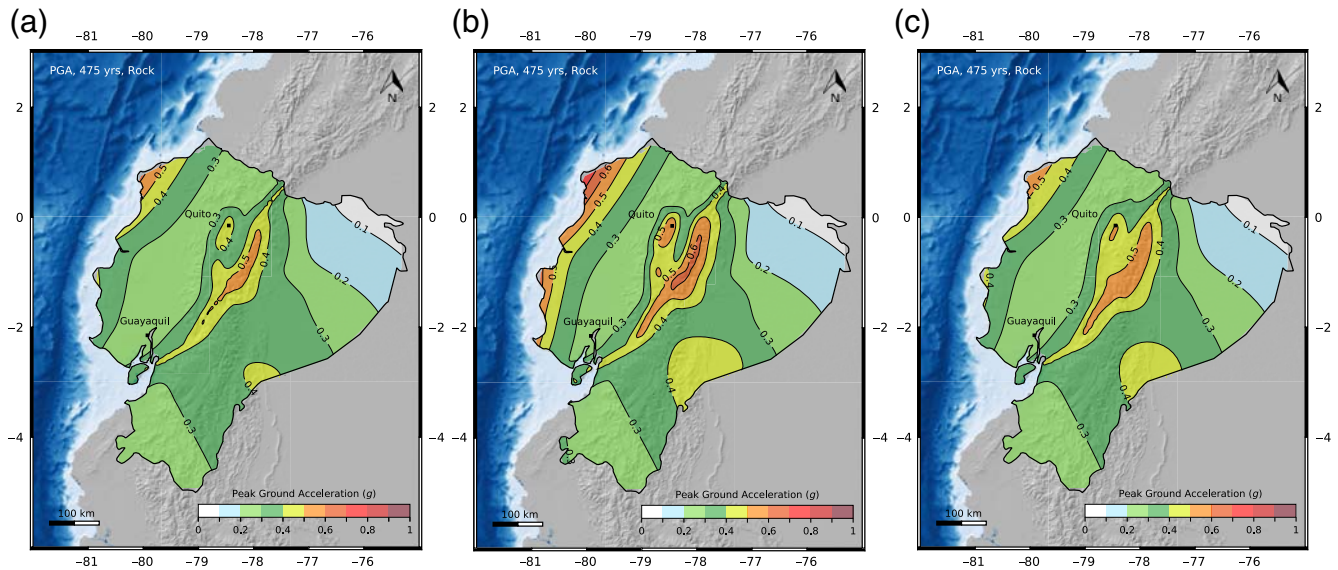

Figure 14. Mean hazard maps, full source logic tree (Fig. 11), only 1 GMM per source type: (a) Abrahamson *et al.* (2016) for interface subduction events, Chiou and Youngs (2014) for crustal events; (b) Montalva *et al.* (2017) for interface events, Akkar *et al.* (2014) for crustal events; and (c) Zhao *et al.* (2006) for interface events and for crustal events. Abrahamson *et al.* (2016) is always used for inslab events. Results for the PGA and for the 475-yr return period are shown. The color version of this figure is available only in the electronic edition.

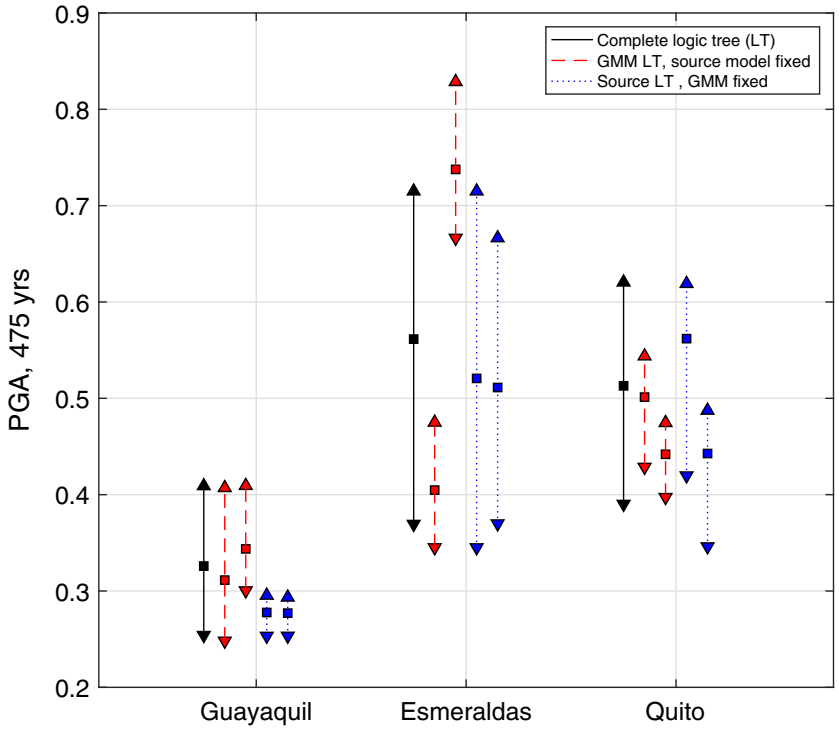

Figure 15. Hazard estimates for the PGA, at 475-yr return period, in three cities: Guayaquil, Esmeraldas, and Quito (see locations in Fig. 13). Three calculations: solid line, exploration of the complete logic tree (source model and GMM logic trees); dashed line, the full GMM logic tree is explored keeping the source model fixed (first calculation with area model based on the BSSA2013 catalog, second calculation with area and crustal faults model based on the ISC-based catalog); dotted line, the full source model logic tree is explored, using a unique selection of GMMs (first calculation with interface Aetal2016, inslab Aetal2016, crustal Akkar *et al.*, 2014; and second calculation with interface Zetal2006, inslab Aetal2016, crustal Chiou and Youngs, 2014). The color version of this figure is available only in the electronic edition.

Conclusions

Based on the work done during the last decade in Ecuador, a source model logic tree is proposed to estimate probabilities of occurrence of subduction and crustal earthquakes that represent a threat to sites in Ecuador. This source model logic tree is made of alternative models: the area model as well as fault and background seismicity models, relying on different types of data and representing, as much as possible, actual knowledge about earthquake occurrences in the country. A set of GMMs is selected to capture the epistemic uncertainty on the prediction of ground motions in Ecuador. Results for different combinations of the logic-tree branches are displayed to understand how the decisions on the source model and the GMM impact the hazard estimates.

Exploring the full logic tree, mean hazard maps show that most of Ecuador is characterized by a high hazard level, with PGA mean values at 475-yr return period higher than $0.3g$ almost everywhere except in some regions of the coastal plain and Amazonia. Regions presenting mean values larger than $0.4g$ are located along the coast and inside the Cordillera. Moreover, the results show that the uncertainty on the hazard estimates depends on the site and can be considerable. The difference between accelerations corresponding to the 16th and 84th percentiles varies from $0g$ to $0.6g$ depending on the location. The uncertainties on the source model and on the GMM both contribute to the overall uncertainty. At the sites where uncertainties on hazard estimates are highest (difference between 84th and 16th percentiles $> 0.4g$), the overall uncertainty is controlled by the epistemic uncertainty on the source model.

Much remains to be done to improve the models and hopefully reduce the uncertainties. The variability of the hazard estimates in the Esmeraldas interface source zone shows that more complex models than the Gutenberg–Richter recurrence model need to be looked for to predict earthquake occurrences in this zone. As for the crustal fault model, it will be possible to define more detailed fault segments only after extensive fieldwork is done to characterize the activity of crustal faults (segmentation, extension in 3D, slip-rate estimates, and past earthquakes). Remoteness and dense jungle coverage of principal segments of many active faults make this task complicated. More data are needed before more realistic time-dependent models can be proposed to predict earthquake occurrence on active faults. The strong-motion dataset is growing and efforts should be put into building a reliable well-organized database, to enable a thorough analysis of the attenuation of ground motions in Ecuador, and comparison tests of recorded ground motions with predictions from published GMMs.

The complete results will be available on the website of the Geophysical Institute in Quito (hazard curves, uniform hazard spectra, and maps for different return periods and different spectral periods).

Data and Resources

The data used in this article are from International Seismological Centre (ISC) online bulletin (http://www.isc.ac.uk/iscbulletin/search/bulletin/, last accessed December 2017); ISC-Global Earthquake Model (GEM) Global Instrumental Earthquake Catalogue v. 4.0 (1900–2013; http://www.isc.ac.uk/iscgem/index.php, last accessed January 2017); National Earthquake Information Center (NEIC) earthquake catalog (https://earthquake.usgs.gov/earthquakes/search/, last accessed June 2017); Global Central Moment Tensor earthquake catalog (http://www.globalcmt.org/CMTsearch.html, all events 1976–2013, catalog available in ASCII "ndk" format, last accessed December 2017); OpenQuake Engine (https://www

.globalquakemodel.org/openquake, last accessed January 2018); and Neotec database (http://neotec-opendata.com/, last accessed December 2017).

Acknowledgments

This work was supported by the Institut de Recherche pour le Développement (IRD), the Geophysical Institute in Quito, part of the Escuela Politecnica Nacional, ISTerre laboratory, and the French National Research Agency through the project REMAKE (2016–2019, Grant Number ANR-15-CE04-004). Instrumentation installed thanks to two projects: SENACYT PIN-08-EPNGEO-00001 (Fortalecimiento del Instituto Geofisico: Ampliacion y Modernizacion del Servicio Nacional de Sismologia Y Vulcanologia) and SENPLADES (Generación de capacidades para la difusión de alertas tempranas y para el desarrollo de instrumentos de decisión ante las amenazas sísmicas y volcánicas dirigidos al Sistema Nacional de Gestión de Riesgos). This work has been carried out in the frame of the Joint International Laboratory "Seismes & Volcans dans les Andes du Nord" (IRD LMI SVAN). The authors are grateful to the Global Earthquake Model Modeling Facility and to the IT ISTerre team for constant support on the OpenQuake software and server. The authors finally thank Associate Editor Mark Stirling, as well as Ivan Wong and an anonymous reviewer, who provided detailed and constructive reviews.

References

Abe, K. (1981). Magnitudes of large shallow earthquakes from 1904 to 1980, *Phys. Earth Planet. In.* **27,** 72–92.

Abe, K., and S. Noguchi (1983). Revision of magnitudes of large shallow earthquakes 1897–1912, *Phys. Earth Planet. In.* **33,** 1–11.

Abrahamson, N., N. Gregor, and K. Addo (2016). BC hydro ground motion prediction equations for subduction earthquakes, *Earthq. Spectra* **32,** no. 1, 23–44.

Akkar, S., M. A. Sandikkaya, and J. J. Bommer (2014). Empirical ground-motion models for point- and extended-source crustal earthquake scenarios in Europe and the Middle East, *Bull. Earthq. Eng.* **12,** no. 1, 359–387.

Aktug, B., J. M. Nocquet, A. Cingöz, B. Parsons, Y. Erkan, P. England, O. Lenk, M. A. Gürdal, A. Kilicoglu, H. Akdeniz, *et al.* (2009). Deformation of western Turkey from a combination of permanent and campaign GPS data: Limits to block-like behavior, *J. Geophys. Res.* **114,** no. B10404, doi: 10.1029/2008JB006000.

Alvarado, A., L. Audin, J. M. Nocquet, E. Jaillard, P. Mothes, P. Jarrín, M. Segovia, F. Rolandone, and D. Cisneros (2016). Partitioning of oblique convergence in the northern Andes subduction zone: Migration history and present-day boundary of the North Andean Sliver in Ecuador, *Tectonics* **35,** doi: 10.1002/2016TC004117.

Alvarado, A., L. Audin, J. M. Nocquet, S. Lagreulet, M. Segovia, Y. Font, G. Lamarque, H. Yepes, P. Mothes, F. Rolandone, *et al.* (2014). Active tectonics in Quito, Ecuador, assessed by geomorphological studies, GPS data, and crustal seismicity, *Tectonics* **33,** no. 2, 67–83, doi: 10.1002/2012TC003224.

Anderson, J. G., and J. E. Luco (1983). Consequences of slip rate constraints on earthquake occurrence relations, *Bull. Seismol. Soc. Am.* **73,** no. 2, 471–496.

Arango, M., F. Strasser, J. Bommer, J. Cepeda, R. Boroschek, D. Hernandez, and H. Tavera (2012). An evaluation of the applicability of current ground-motion models to the south and central American subduction zones, *Bull. Seismol. Soc. Am.* **102,** 143–168.

Audin, L., L. Torlay, H. Castro, J. Aguilar, S. Debard, C. Benavente, and A. Alvarado (2014). Neotec Open-data Base de données "Neotectonica" en open access: Failles Actives en Amérique du Sud, Conférence SAGEO, "Innovations géomatiques pour la gestion des risques naturels et technologiques", http://www.neotec-opendata.com (last accessed March 2018) (in French).

Baize, S., L. Audin, T. Winter, A. Alvarado, L. Pilatasig Moreno, M. Taipe, P. Reyes, P. Kauffman, and H. Yepes (2015). Paleoseismology and tectonic geomorphology of the Pallatanga fault (central Ecuador), a major structure of the South-American crust, *Geomorphology* **237,** 14–28, doi: 10.1016/j.geomorph.2014.02.030.

Beauval, C., F. Cotton, N. Abrahamson, N. Theodulidis, E. Delavaud, L. Rodriguez, F. Scherbaum, and A. Haendel (2012). Regional differences in subduction ground motions, *World Conference on Earthquake Engineering*, Lisbon, Portugal, 24–28 September, 10 pp.

Beauval, C., J. Marinière, A. Laurendeau, J.-C. Singaucho, C. Viracucha, M. Vallée, E. Maufroy, D. Mercerat, H. Yepes, M. Ruiz, *et al.* (2017). Comparison of observed ground-motion attenuation for the 16 April 2016 M_w 7.8 Ecuador megathrust earthquake and its two largest aftershocks with existing ground-motion prediction equations, *Seismol. Res. Lett.* **88,** no. 2A, 287–299.

Beauval, C., H. Tasan, A. Laurendeau, E. Delavaud, F. Cotton, P. Guéguen, and N. Kuehn (2012). On the testing of ground-motion prediction equations against small magnitude data, *Bull. Seismol. Soc. Am.* **102,** no. 5, 1994–2007.

Beauval, C., H. Yepes, L. Audin, A. Alvarado, J.-M. Nocquet, D. Monelli, and L. Danciu (2014). Probabilistic seismic hazard assessment in Quito, estimates and uncertainties, *Seismol. Res. Lett.* **85,** no. 6, doi: 10.1785/0220140036.

Beauval, C., H. Yepes, W. Bakun, J. Egred, A. Alvarado, and J.-C. Singaucho (2010). Locations and magnitudes of historical earthquakes in the Sierra of Ecuador (1587-1996), *Geophys. J. Int.* **181,** no. 3, 1613–1633, doi: 10.1111/j.1365-246X.2010.04569.x.

Beauval, C., H. Yepes, P. Palacios, M. Segovia, A. Alvarado, Y. Font, J. Aguilar, L. Troncoso, and S. Vaca (2013). An earthquake catalog for seismic hazard assessment in Ecuador, *Bull. Seismol. Soc. Am.* **103,** 773–786, doi: 10.1785/0120120270.

Bès de Berc, S., J. C. Soula, P. Baby, M. Souris, F. Christophoul, and J. Rosero (2005). Geomorphic evidence of active deformation and uplift in a modern continental wedge-top–foredeep transition: Example of the eastern Ecuadorian Andes, *Tectonophysics* **399,** 351–380, doi: 10.1016/j.tecto.2004.12.030.

Bindi, D., M. Massa, L. Luzi, G. Ameri, F. Pacor, R. Puglia, and P. Augliera (2014). Pan-European ground motion prediction equations for the average horizontal component of PGA, PGV and 5%-damped PSA at spectral periods of up to 3.0 s using the RESORCE dataset, *Bull. Earthq. Eng.* **12,** no. 1, 391–430.

Bonilla, L. F., M. C. Ruiz, and H. Yepes (1992). Evaluation of seismic hazard in Ecuador, *Simposio Internacional sobre Prevención de Desastres Sísmicos, Mem.*, UNAM, Mexico, 118–125.

Boore, D. M., J. P. Stewart, E. Seyhan, and G. Atkinson (2014). NGA-West2 equations for predicting PGA, PGV, and 5% damped PGA for shallow crustal earthquakes, *Earthq. Spectra* **30,** no. 3, 1057–1085.

Código Ecuatoriano de la Construcción (CEC) (2001). *Requisitos generales de diseño: Peligro sísmico, espectros de diseño y requisitos mínimos de cálculo para diseño sismo-resistente*, Instituto Ecuatoriano de Normalización (INEN), Quito, Ecuador, 1–32 (in Spanish).

Chiou, B. S.-J, and R. Youngs (2014). Updated of the Chiou and Youngs NGA model for the average horizontal component of peak ground motion and response spectra, *Earthq. Spectra* **30,** no. 3, 1117–1153.

Chlieh, M., P. A. Mothes, J.-M. Nocquet, P. Jarrin, P. Charvis, D. Cisneros, Y. Font, J.-Y. Collot, J.-C. Villegas-Lanza, F. Rolandone, *et al.* (2014). Distribution of discrete seismic asperities and aseismic slip along the Ecuadorian megathrust, *Earth Planet. Sci. Lett.* **400,** 292–301, doi: 10.1016/j.epsl.2014.05.027.

Chuang, Y., and K. M. Johnson (2011). Reconciling geologic and geodetic model fault slip-rate discrepancies in southern California: Consideration of nonsteady mantle flow and lower crustal fault creep, *Geology* **39,** 627–630, doi: 10.1130/G32120.1.

Collot, J.-Y., E. Sanclemente, J.-M. Nocquet, A. Leprêtre, A. Ribodetti, P. Jarrin, M. Chlieh, D. Graindorge, and P. Charvis (2017). Subducted oceanic relief locks the shallow megathrust in central Ecuador, *J. Geophys. Res.* doi: 10.1002/2016JB013849.

Cornell, C. A. (1968). Engineering seismic risk analysis, *Bull. Seismol. Soc. Am.* **58,** no. 1, 1583–1606.

Delavaud, E., F. Cotton, S. Akkar, F. Scherbaum, L. Danciu, C. Beauval, S. Drouet, J. Douglas, R. Basili, M. A. Sandikkaya, *et al.* (2012). Toward a ground-motion logic tree for probabilistic seismic hazard assessment in Europe, *J. Seismol.* doi: 10.1007/s10950-012-9281-z.

Di Giacomo, D., I. Bondár, D. A. Storchak, E. R. Engdahl, P. Bormann, and J. Harris (2015). ISC-GEM: Global instrumental earthquake catalog (1900–2009): III. Re-computed M_s and m_b, proxy M_w, final magnitude composition and completeness assessment, *Phys. Earth Planet. In.* **239,** 33–47, doi: 10.1016/j.pepi.2014.06.005.

Douglas, J., and B. Edwards (2016). Recent and future developments in earthquake ground motion estimation, *Earth Sci. Rev.* **160,** 203–219.

Drouet, S., G. Montalva, M. C. Dimaté, L. F. Castillo, G. A. Fernandez, C. Morales, N. Bastias, M. Pirchiner, J. C. Singaucho, and G. Weatherhill (2017). Building a ground-motion logic tree for South America within the GEM-SARA project framework, *16th World Conference on Earthquake Engineering*, Santiago, Chile, 9–13 January, Paper Number 2759, 12 pp.

Dumont, J. F., E. Santana, W. Vilema, K. Pedoja, M. Ordóñez, M. Cruz, N. Jiménez, and I. Zambrano (2005). Morphological and microtectonic analysis of Quaternary deformation from Puná and Santa Clara Islands, Gulf of Guayaquil, Ecuador (South America), *Tectonophysics* **399,** nos. 1/4, 331–350, doi: 10.1016/j.tecto.2004.12.029.

Dziewonski, A. M., T.-A. Chou, and J. H. Woodhouse (1981). Determination of earthquake source parameters from waveform data for studies of global and regional seismicity, *J. Geophys. Res.* **86,** 2825–2852, doi: 10.1029/JB086iB04p02825.

Ego, F., and M. Sebrier (1996). The Ecuadorian Inter-Andean valley: A major and complex restraining bend and compressive graben since Late Miocene time, *Ann. Tect.* **10,** nos. 1/2, 31–59.

Ego, F., M. Sébrier, A. Lavenu, H. Yepes, and A. Egüez (1996). Quaternary state of stress in the northern Andes and the restraining bend model for the Ecuadorian Andes, *Tectonophysics* **259,** nos. 1/3, 101–116.

Ego, F., M. Sébrier, and H. Yepes (1995). Is the Cauca-Patia and Romeral fault system left or right lateral? *Geophys. Res. Lett.* **22,** 33–36.

Ekström, G., M. Nettles, and A. M. Dziewonski (2012). The Global CMT project 2004–2010: Centroid-moment tensors for 13,017 earthquakes, *Phys. Earth Planet. In.* **200/201,** 1–9.

Esteva, L. (1968). Bases para la formulacion de decisiones de diseño sismico, *Ph.D. Thesis* and *Report 182*, Universidad Autonoma Nacional de Mexico (in Spanish).

Eurocode 8 (2004). Design of structures for earthquake resistance—Part 1: General rules, seismic actions and rules for buildings, EN 1998–1, European Committee for Standardization, Brussels, Belgium.

Fiorini, E., and A. Tibaldi (2012). Quaternary tectonics in the central Interandean Valley, Ecuador: Fault-propagation folds, transfer faults and the Cotopaxi volcano, *Global Planet. Change* **90/91,** 87–103, doi: 10.1016/j.gloplacha.2011.06.002.

Fukushima, Y. (1997). Comment on "Ground Motion Attenuation Relations for Subduction Zones," *Seismol. Res. Lett.* **68,** 947–949.

Garcia, J., G. Weatherhill, M. Pagani, L. Rodriguez, V. Poggi, and the SARA Hazard Working Group (2017). Building an open seismic hazard model for South America: The SARA-PSHA model, *16th World Conference on Earthquake Engineering*, Santiago, Chile, 9–13 January, Paper Number 2145, 13 pp.

Global Earthquake Model (GEM) (2017). The OpenQuake-engine User Manual, *Global Earthquake Model (GEM) Technical Report 201710*, 187 pp.

Gutenberg, B., and F. Richter (1944). Frequency of earthquakes in California, *Bull. Seismol. Soc. Am.* **34,** 185–188.

Gutenberg, B., and C. F. Richter (1965). *Seismicity of the Earth and Associated Phenomena*, Princeton University Press, Princeton, New Jersey, 1954; reprinted, Stechert-Hafner.

Kanamori, H., and K. C. McNally (1982). Variable rupture mode of the subduction zone along the Ecuador-Colombia coast, *Bull. Seismol. Soc. Am.* **72,** no. 4, 1241–1253.

Lavenu, A., T. Winter, and F. Dávila (1995). A Pliocene-Quaternary compressional 899 basin in the Interandean depression, central Ecuador, *Geophys. J. Int.* **121,** 279–300.

Leonard, M. (2010). Earthquake fault scaling: Relating rupture length, width, average displacement, and moment release, *Bull. Seismol. Soc. Am.* **100,** no. 5A, 1971–1988.

Lolli, B., P. Gasperini, and G. Vannucci (2014). Empirical conversion between teleseismic magnitudes (m_b and M_s) and moment magnitude (M_w) at the Global, Euro-Mediterranean and Italian scale, *Geophys. J. Int.* **199,** 805–828.

Monelli, D., M. Pagani, G. Weatherill, L. Danciu, and J. Garcia (2014). Modeling distributed seismicity for probabilistic seismic-hazard analysis: Implementation and insights with the OpenQuake Engine, *Bull. Seismol. Soc. Am.* doi: 10.1785/0120130309.

Montalva, G., N. Bastias, and A. Rodriguez-Marek (2017). Ground-motion prediction equation for the Chilean subduction zone, *Bull. Seismol. Soc. Am.* **107,** no. 2, doi: 10.1785/0120160221.

Nocquet, J.-M., P. Jarrin, M. Vallée, P. A. Mothes, R. Grandin, F. Rolandone, B. Delouis, H. Yepes, Y. Font, D. Fuentes, *et al.* (2016). Supercycle at the Ecuadorian subduction zone revealed after the 2016 Pedernales earthquake, *Nature Geosci.* doi: 10.1038/ngeo2864.

Nocquet, J.-M., J. C. Villegas-Lanza, M. Chlieh, P. A. Mothes, F. Rolandone, P. Jarrin, D. Cisneros, A. Alvarado, L. Audin, F. Bondoux, *et al.* (2014). Continental deformation and creeping subduction in the Northern Andes, *Nature Geosci.* **7,** 287–291.

Norma Ecuatoriana de la Construcción (NEC) (2015). Norma Ecuatoriana de la Construcción, Sub-capítulo 2, *Peligro Sísmico y Requisitos de Diseño Sismo Resistente*, Ministerio de Desarrollo Urbano y Vivienda, Convenio MIDUVI-Cámara de la Construcción de Quito, 1–139 (in Spanish).

Pacheco, J. F., and L. R. Sykes (1992). Seismic moment catalog of large shallow earthquakes, 1900 to 1989, *Bull. Seismol. Soc. Am.* **82,** 1306–1349.

Pagani, M., D. Monelli, G. Weatherill, L. Danciu, H. Crowley, V. Silva, P. Henshaw, L. Butler, M. Nastasi, L. Panzeri, *et al.* (2014). OpenQuake-engine: An open hazard (and risk) software for the global earthquake model, *Seismol. Res. Lett.* **85,** 692–702.

Pagani, M., D. Monelli, G. A. Weatherill, and J. Garcia (2014). The OpenQuake-engine Book: Hazard, *Global Earthquake Model (GEM) Technical Report 2014-08*, 67 pp.

Petersen, M. D., M. P. Moschetti, P. M. Powers, C. S. Mueller, K. M. Haller, A. D. Frankel, Y. Zeng, S. Rezaeian, S. C. Harmsen, O. S. Boyd, *et al.* (2014). Documentation for the 2014 update of the United States national seismic hazard maps, *U.S. Geol. Surv. Open-File Rept. 2014-1091*, 243 pp., doi: 10.3133/ofr20141091.

Polonia, A., L. Gasperini, A. Amorosi, E. Bonatti, G. Bortoluzzi, N. Cagatay, L. Capotondi, M. H. Cormier, N. Gorur, C. McHugh, *et al.* (2004). Holocene slip rate of the North Anatolian fault beneath the Sea of Marmara, *Earth Planet. Sci. Lett.* **227,** 411–426, doi: 10.1016/j.epsl.2004.07.042.

Scherbaum, F., E. Delavaud, and C. Riggelsen (2009). Model selection in seismic hazard analysis: An information-theoretic perspective, *Bull. Seismol. Soc. Am.* **99,** no. 6, 3234–3247.

Scordilis, E. M. (2006). Empirical global relations converting M_s and m_b to moment magnitude, *J. Seismol.* **10,** 225–236.

Smith-Konter, B., D. Sandwell, and P. Shearer (2011). Locking depths estimated from geodesy and seismology along the San Andreas Fault System: Implications for seismic moment release, *J. Geophys. Res.* **116,** no. B06401, doi: 10.1029/2010JB008117.

Stewart, J. P., J. Douglas, M. Javanbarg, N. A. Abrahamson, Y. Bozorgnia, D. M. Boore, K. W. Campbell, E. Delavaud, M. Erdik, and P. J. Stafford (2015). Selection of ground motion prediction equations for the global earthquake model, *Earthq. Spectra* doi: 10.1193/013013EQS017M.

Storchak, D. A., D. Di Giacomo, E. R. Engdahl, J. Harris, I. Bondár, W. H. K. Lee, P. Bormann, and A. Villaseñor (2015). The ISC-GEM Global Instrumental Earthquake Catalog (1900–2009): Introduction, *Phys. Earth Planet. In.* **239,** 48–63, doi: 10.1016/j.pepi.2014.06.009.

Strasser, F. O., M. C. Arango, and J. J. Bommer (2010). Scaling of the source dimensions of interface and intraslab subduction-zone earthquakes with moment magnitude, *Seismol. Res. Lett.* **81,** 941–950.

Taboada, A., L. A. Rivera, A. Fuenzalida, A. Cisternas, H. Philip, H. Bijwaard, J. Olaya, and C. Rivera (2000). Geodynamics of the northern Andes: Subductions and intracontinental deformation (Colombia), *Tectonics* **19,** 787–813.

Tibaldi, A., A. Rovida, and C. Corazzato (2007). Late Quaternary kinematics, slip-rate and segmentation of a major Cordillera-parallel transcurrent fault: The Cayambe-Afiladores-Sibundoy system, NW South America, *J. Struct. Geol.* **29,** no. 4, 664–680, doi: 10.1016/j.jsg.2006.11.008.

Vallée, M., J. M. Nocquet, J. Battaglia, Y. Font, M. Segovia, M. Régnier, P. Mothes, P. Jarrin, D. Cisneros, S. Vaca, *et al.* (2013). Intense interface seismicity triggered by a shallow slow slip event in the central Ecuador subduction zone, *J. Geophys. Res.* **118,** 2965–2981, doi: 10.1002/jgrb.50216.

Villegas-Lanza, J. C., M. Chlieh, O. Cavalie, H. Tavera, P. Baby, J. Chire-Chira, and J. M. Nocquet (2016). Active tectonics of Peru: Heterogeneous interseismic coupling along the Nazca megathrust, rigid motion of the Peruvian Sliver, and Subandean shortening accommodation, *J. Geophys. Res.* **121,** no. 10, 7371–7394, ISSN 2169–9313.

Weichert, D. H. (1980). Estimation of the earthquake recurrence parameters for unequal observation periods for different magnitudes, *Bull. Seismol. Soc. Am.* **70,** no. 4, 1337–1346.

Winter, T., J. P. Avouac, and A. Lavenu (1993). Late Quaternary kinematics of the Pallatanga strike-slip fault (Central Ecuador) from topographic measurements of displaced morphological features, *Geophys. J. Int.* **115,** no. 3, 905–920.

Witt, C., J. Bourgois, F. Michaud, M. Ordonez, N. Jimenez, and M. Sosson (2006). Development of the Gulf of Guayaquil (Ecuador) during the Quaternary as an effect of the North Andean block tectonic escape, *Tectonics* doi: 10.1029/2004TC001723.

Woessner, J., L. Danciu, D. Giardini, H. Crowley, F. Cotton, G Grünthal, G. Valensise, R. Arvidsson, R. Basili, M. B. Demircioglu, *et al.* (2015). The 2013 European seismic hazard model: Key components and results, *Bull. Earthq. Eng.* **13,** no. 12, 3553–3596, doi: 10.1007/s10518-015-9795-1.

Ye, L., H. Kanamori, J.-P. Avouac, L. Li, K.-F. Cheung, and T. Lay (2016). The 16 April 2016, M_w 7.8 (M_s 7.5) Ecuador earthquake: A quasi-repeat of the 1942 M_s 7.5 earthquake and partial re-rupture of the 1906 M_s 8.6 Colombia-Ecuador earthquake, *Earth Planet. Sci. Lett.* doi: 10.1016/j.epsl.2016.09.006.

Yepes, H., L. Audin, A. Alvarado, C. Beauval, J. Aguilar, Y. Font, and F. Cotton (2016). A new view for the geodynamics of Ecuador: Implication in seismogenic source definition and seismic hazard assessment, *Tectonics* **35,** doi: 10.1002/2015TC003941.

Zhao, J. X., X. Liang, F. Jiang, H. Xing, Y. Zhang, C. Zhao, X. Lan, D. A. Rhoades, P. G. Somerville, K. Irikura, *et al.* (2016). Ground-motion prediction equations for subduction interface earthquakes in Japan using site class and simple geometric attenuation functions, *Bull. Seismol. Soc. Am.* **106,** no. 4, doi: 10.1785/0120150034.

Zhao, J. X., J. Zhang, A. Asano, Y. Ohno, T. Oouchi, T. Takahashi, H. Ogawa, K. Irikura, H. K. Thio, P. G. Somerville, *et al.* (2006). Attenuation relations of strong ground motion in Japan using site classification based on predominant period, *Bull. Seismol. Soc. Am.* **96,** no. 3, 898–913.

Université Grenoble Alpes, Université Savoie Mont Blanc, CNRS, IRD, IFSTTAR, ISTerre
38000 Grenoble
France
celine.beauval@univ-grenoble-alpes.fr
(C.B., J.M., L.A.)

Escuela Politécnica Nacional
Instituto Geofísico
Ladrón de Guevara E11-253
Apartado 2759 Quito, Ecuador
(H.Y., A.A., J.A., J.-C.S.)

Geoazur, Université Côte d'Azur, IRD, CNRS, Observatoire de la Côte d'Azur
Campus CNRS Azur, 250 rue A. Einstein
Valbonne, France
(J.-M.N.)

Institut de Radioprotection et Sûreté Nucléaire
BP17, 92262 Fontenay-aux-Roses
France
(S.B., H.J.)

Manuscript received 9 September 2017;
Published Online 3 April 2018